







Optical and JWST Mid-IR Emission Line Diagnostics for Simultaneous IMBH and Stellar Excitation in $z \sim 0$ Dwarf Galaxies*

Chris T. Richardson^{1,2} , Connor Simpson¹, Mugdha S. Polimera³ , Sheila J. Kannappan³ , Jillian M. Bellovary^{4,5,6} , Christopher Greene⁷, and Sam Jenkins¹

¹Elon University, 100 Campus Drive, Elon, NC 27278, USA; crichardson17@elon.edu

²COSmS Institute, University of North Carolina, Chapel Hill, NC 27599, USA

³University of North Carolina, 141 Chapman Hall CB 3255, Chapel Hill, NC 27599, USA

⁴Queensborough Community College, City University of New York, 222-05 56th Ave, Bayside, NY 11364, USA

⁵American Museum of Natural History, Central Park West at 79th Street, New York, NY 10024, USA

⁶Graduate Center, City University of New York, New York, NY 10016, USA

⁷University of Cincinnati, 290 CCM Blvd, Cincinnati, OH 45221, USA

Received 2021 August 4; revised 2022 January 19; accepted 2022 January 31; published 2022 March 14

Abstract

Current observational facilities have yet to conclusively detect 10^3 – $10^4 M_\odot$ intermediate-mass black holes (IMBHs) that fill in the evolutionary gap between seed black holes in the early universe and $z \sim 0$ supermassive black holes. Dwarf galaxies present an opportunity to reveal active IMBHs amidst persistent star formation. We introduce photoionization simulations tailored to address key physical uncertainties: coincident versus noncoincident mixing of IMBH and starlight excitation, open versus closed geometries of surrounding gas clouds, and different shapes of the spectral energy distribution of active galactic nuclei (AGN). We examine possible AGN emission line diagnostics in the optical and mid-IR, and find that the diagnostics are often degenerate with respect to the investigated physical uncertainties. In spite of these setbacks, and in contrast to recent work, we are able to show that $[\text{O III}]/\text{H}\beta$ typically remains bright for dwarf AGN powered by IMBHs down to $10^3 M_\odot$. Dwarf AGN are predicted to have inconsistent star-forming and Seyfert/LINER classifications using the most common optical diagnostics. In the mid-IR, $[\text{O IV}] 25.9 \mu\text{m}$ and $[\text{Ar II}] 6.98 \mu\text{m}$ are less sensitive to physical uncertainties than are optical diagnostics. Based on these emission lines, we provide several diagrams of mid-IR emission line diagnostic diagrams with demarcations for separating starbursts and AGN with varying levels of activity. The diagrams are valid over a wide range of ionization parameters and metallicities out to $z \sim 0.1$, so will prove useful for future JWST observations of local dwarf AGN in the search for IMBHs. We make our photoionization simulation suite freely available.

Unified Astronomy Thesaurus concepts: Dwarf galaxies (416); Active galactic nuclei (16); Intermediate-mass black holes (816); Starburst galaxies (1570); Emission line galaxies (459)

1. Introduction

The occupation fraction of supermassive black holes (SMBHs) in massive galaxies is near unity (Magorrian et al. 1998). While LIGO and VIRGO have detected stellar-mass black holes ($\leq 10^2 M_\odot$) resulting from compact object mergers, intermediate-mass black holes (IMBHs) remain elusive in the 10^2 – $10^5 M_\odot$ range (Greene et al. 2020). Detecting black holes at the low end of this range would provide a crucial link between black hole seeds in the early universe and local SMBHs.

Dwarf galaxies show promise in the search for IMBHs based on the M_* – M_{BH} relation (Reines & Volonteri 2015). However, the properties of dwarf hosts of active galactic nuclei (AGN) are different from those of massive galaxy AGN hosts, which can complicate detecting AGN signatures. For example, most dwarfs are gas-rich (Kannappan 2004), strongly star-forming (Geha et al. 2012), and metal-poor (Tremonti et al. 2004). Supernova feedback preferentially expels metal-rich gas

(Mac Low & Ferrara 1999), while accretion of low-metallicity gas from the intergalactic medium drives star formation (Dekel & Birnboim 2006).

Unlike in the unified AGN model, IMBHs in dwarfs often wander within 1 kpc of the center due to the dwarfs' weak gravitational potential (Reines et al. 2020; Bellovary et al. 2021). Therefore, it is unclear whether the AGN and stellar radiation fields strike the same gas clouds or spatially separated gas clouds as the IMBH relocates or settles down in a particular location. This uncertainty calls into question the application of the centralized geometric model for massive AGN to dwarf AGN.

Another issue for dwarf AGN, unlike massive AGN, is that X-ray observations that could provide valuable constraints on the AGN spectral energy distribution (SED) remain rare for $M_{\text{BH}} \approx 10^5 M_\odot$ and absent for $M_{\text{BH}} \approx 10^3 M_\odot$ (Desroches et al. 2009). The few sources luminous enough to observe are likely outliers having fortuitous conditions to enable their detection (e.g., Godet et al. 2012). This situation introduces doubts about whether physical quantities controlling the shape of the SED scale down to the lowest black hole masses (Arcodia et al. 2020).

Photoionization models can provide the missing ingredient for IMBH detection by systematically accounting for uncertainties pertaining to the gaseous geometry and properties of low-mass AGN. The left panels of Figure 1 illustrate open, or plane-parallel geometries, where the covering factor is small, as

* Released on XXXX, XXXX, 2021

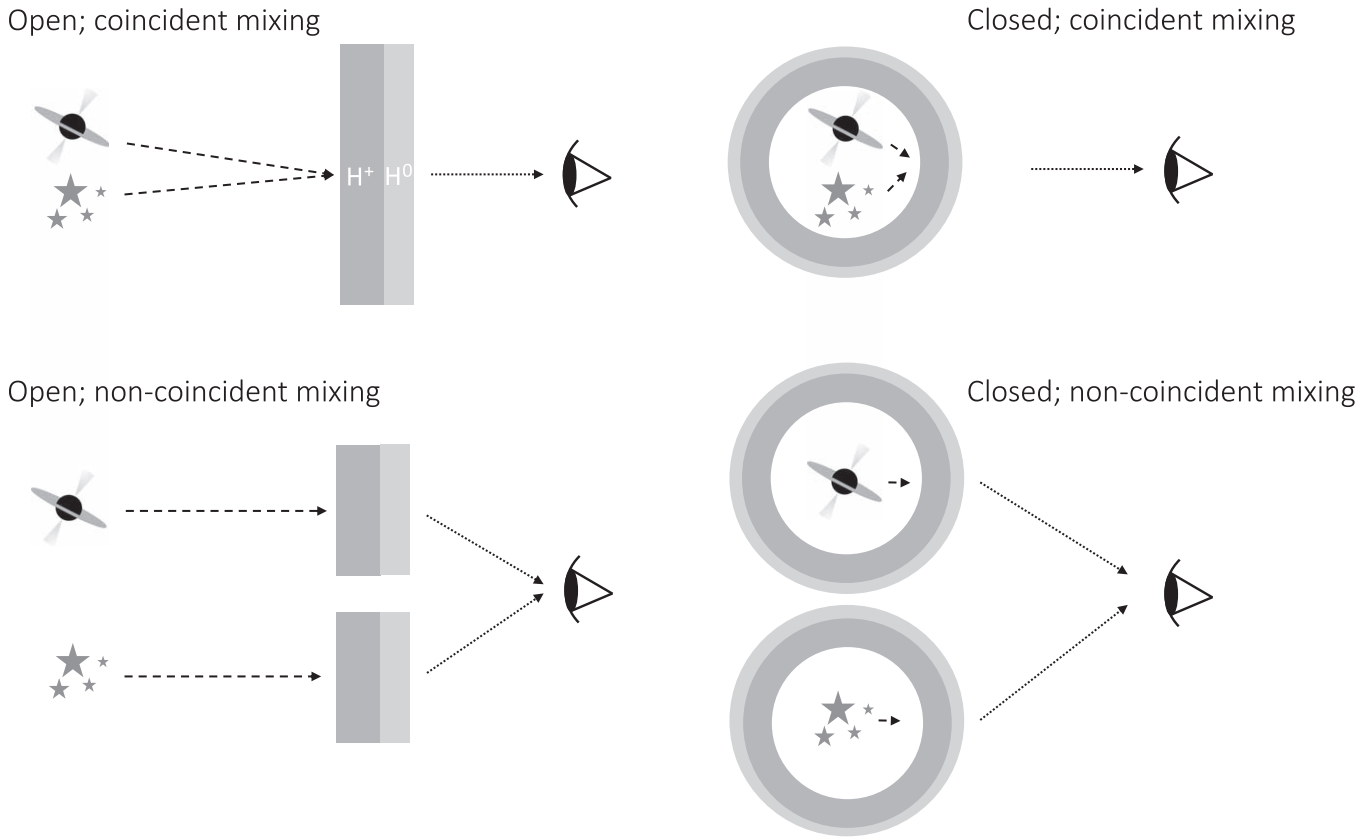


Figure 1. Illustration depicting two different gas cloud geometries (open and closed) and two different mixing methodologies (coincident and noncoincident). Dwarf AGN could presumably fall into any of these four categories, and therefore photoionization models must account for this systematic uncertainty. Note that the rays of light (arrows) only show one possible path to the observer and do not represent all possible components of the observed spectrum.

typically assumed when modeling AGN (Elvis 2000; Feltre et al. 2016) and star-forming regions like the Orion blister (Ferland 2001). The right panels of Figure 1 illustrate closed or spherical geometries, where the covering factor is close to unity, as typically assumed when modeling obscured AGN-like ULIRGs (Abel et al. 2009) and star-forming regions like 30 Doradus (Pellegrini et al. 2011).

Similarly, photoionization models have used two methods to take into account simultaneous AGN and stellar excitation, but rarely with justification. The top panels of Figure 1 illustrate one approach, where an AGN and starlight strike the same cloud, and thus the SEDs from each source are mixed a priori (e.g., Abel et al. 2009; Satyapal et al. 2018), which we label as *coincident mixing*. The bottom panels of Figure 1 show another approach, where the excitation sources illuminate spatially separated clouds, and thus the models are mixed a posteriori (e.g., Kewley et al. 2013; Meléndez et al. 2014; Richardson et al. 2014), which we label as *noncoincident mixing*. Since dwarfs hosting IMBHs display a variety of morphologies (Kimbrell et al. 2021), it is unclear whether a particular gas geometry or mixing methodology would generically apply. Therefore, assessing all possibilities in Figure 1 is paramount.

Optical spectroscopy enables the categorization of emission line galaxies as AGN, star-forming, or a mixture of the two using [O III] $\lambda 5007/H\beta$ against [N II] $\lambda 6584/H\alpha$ (i.e., the BPT diagram), [S II] $\lambda 6720/H\alpha$, and [O I] $\lambda 6300/H\alpha$ to form diagnostic diagrams (Baldwin et al. 1981; Veilleux & Osterbrock 1987). Previous photoionization modeling including AGN suggests that optical lines might grow too faint for detection for black holes outside 10^6 – $10^9 M_\odot$, thus skewing M_{BH} distributions

(Cann et al. 2019; Bhat et al. 2020); however, none of this modeling accounts for the multiple geometrical configurations indicated in Figure 1, for the presence of stellar excitation, or for the uncertainty in the shape of the IMBH SED.

Indeed, optical observations may contradict the theoretical impossibility of detection of IMBH AGN. Broad-line selected dwarf AGN with $M_{\text{BH}} \approx 10^5 M_\odot$ can sometimes be optically classified as AGN using the BPT diagram (Barth et al. 2004), indicating high [O III]/ $H\beta$. Reines et al. (2020) used radio interferometry to identify dwarf AGN classified as optical star-forming galaxies, and used the M_* – M_{BH} relation to deduce $M_{\text{BH}} \sim 10^{4.1}$ – $10^{5.8} M_\odot$, although this relation shows up to 1.0 dex scatter for $M_* < 10^9 M_\odot$ (Greene et al. 2020). Optically classified star-forming galaxies might contain a treasure trove of additional hidden IMBHs that evade detection on account of the BPT diagram preferentially identifying high-metallicity AGN (M. S. Polimera et al., submitted; hereafter P21). However, active black holes in the $10^3 M_\odot$ regime still remain undetected.

IR spectroscopy offers a better opportunity to reliably detect IMBHs because it possesses a wealth of high ionization lines insensitive to gas metallicity and dust extinction. The Spitzer era revealed the potential of the mid-IR to separate starbursts from AGN, leading to the development of several diagnostic diagrams involving [Ne V] and [O IV] emission lines and polycyclic aromatic hydrocarbon (PAH) features (Dale et al. 2006). The James Webb Space Telescope (JWST), spanning 0.6–28.3 μm , has the potential to revolutionize the search for black holes at the low-mass end of the IMBH distribution. Indeed, recent work has shown the spectral range of JWST can

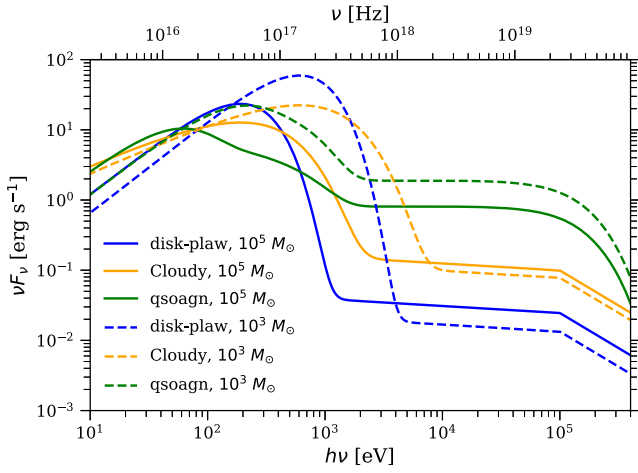


Figure 2. AGN SEDs resulting from different models for $M_{\text{BH}} = 10^3\text{--}10^5 M_{\odot}$. Profound differences are present for the peak of the thermal accretion disk and the hard X-ray contribution.

uncover AGN eluding detection from optical spectroscopy (Satyapal et al. 2021), although the uncertainties stemming from the IMBH SED and the configurations presented in Figure 1 remain unexplored.

In this paper, we fill in the gap in photoionization modeling to account for the uncertainty in gaseous geometry, mixed excitation, and AGN SED shape. We make emission line predictions that will be valuable for searching for $10^3\text{--}10^5 M_{\odot}$ black holes with optical spectroscopy and future JWST observations, while freely providing our simulation suite to the community.⁸

2. Theoretical Methodology

2.1. Incident Radiation Field

Figure 2 displays the three different models for the AGN SED that we have explored, assuming $M_{\text{BH}} = 10^3\text{--}10^5 M_{\odot}$: “disk-plaw,” “Cloudy,” and “qsoagn.” The “disk-plaw” SED combines the `diskbb` accretion disk model (Mitsuda et al. 1984) with a power law ($\Gamma = 2.1$), normalized to give $\alpha_{\text{ox}} = 1.41$ (Grupe et al. 2010) where

$$\frac{f_{\nu}(2 \text{ keV})}{f_{\nu}(2500 \text{ \AA})} = \left(\frac{\nu_{2 \text{ keV}}}{\nu_{2500 \text{ \AA}}} \right)^{\alpha_{\text{ox}}}. \quad (1)$$

The inner `diskbb` temperature is calculated using Peterson (1997):

$$T_{\text{in}} = 6.3 \times 10^5 \left(\frac{\dot{m}}{\dot{m}_{\text{Edd}}} \right)^{1/4} \left(\frac{M_{\text{BH}}}{10^8 M_{\odot}} \right)^{-1/4} \left(\frac{R}{R_{\text{g}}} \right)^{-3/4} \text{ K} \quad (2)$$

where we assume $\dot{m}/\dot{m}_{\text{Edd}} = 0.1$ and $R = 3R_{\text{g}}$. The result is a piecewise, physically motivated SED for photoionization modeling (Cann et al. 2019; Bhat et al. 2020), but lacks physical self-consistency, such as the accretion disk radiation generating seed photons for the hard X-ray component.

The “Cloudy” SED is the `Cloudy` (Ferland et al. 2017) default AGN SED, which is an empirical model that assumes the observed SED is the same as the continuum seen by nebular

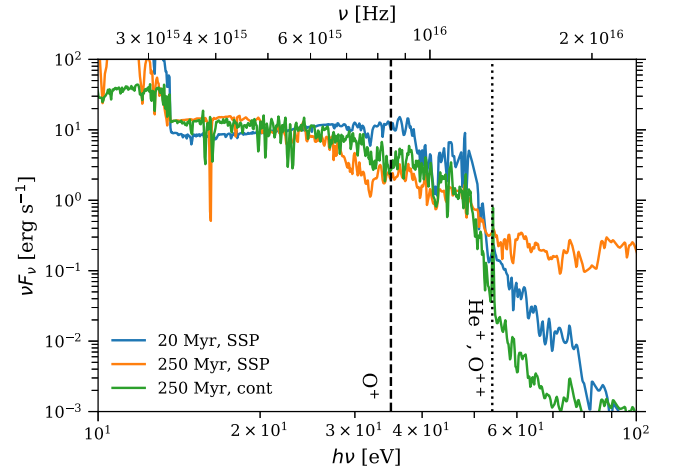


Figure 3. Stellar SEDs resulting from different SFHs. The ionization potentials for relevant species are denoted by vertical lines.

clouds. The functional form of the SED is given by

$$f_{\nu} = \nu^{\alpha_{\text{UV}}} e^{-\frac{h\nu}{kT_{\text{peak}}}} e^{-\frac{kT_{\text{IR}}}{h\nu}} + a\nu^{\alpha_{\text{X}}} \quad (3)$$

where $T_{\text{peak}} = 0.77 T_{\text{in}}$ (Mitsuda et al. 1984), α_{UV} is the low-energy slope in the UV, α_{X} is the X-ray slope, and a is a constant adjusted to satisfy α_{ox} . All of the spectral indices are taken from the median of the extinction-corrected BLS1s sample in Grupe et al. (2010).

The “qsoagn” uses the `AGNed` model (Kubota & Done 2018), while fixing most parameters to their “typical” values and assuming $\dot{m}/\dot{m}_{\text{Edd}} = 0.1$, $a_{*} = 0$, and $i = 45^{\circ}$. This is a physically self-consistent SED for photoionization modeling (Panda et al. 2019; Sarkar et al. 2021) appropriate for sub-Eddington accretion in IMBHs.

Figure 2 shows profound differences between the three SED models. In part, the differences are due to the self-consistent physics in the `qsoagn` that is not featured in the other two models. The `qsoagn` selects the inner accretion disk radius needed to power the X-ray emission and then truncates the disk at that point, rather than arbitrarily selecting $R_{\text{in}} = 6GM/c^2$. This results in the `qsoagn` SED for $M_{\text{BH}} = 10^3 M_{\odot}$ having approximately the same peak energy as the other two SEDs for $M_{\text{BH}} = 10^5 M_{\odot}$, and also a more appreciable hard X-ray component. Throughout the remainder of the paper, we only use the two SEDs that represent extremes: `disk-plaw` and `qsoagn`.

To model the starburst continuum, we use the binary stellar population synthesis (SPS) code `BPASS v2.0` (Stanway et al. 2016) to predict the spectrum emitted from stars subject to binary evolution. Including binaries is essential for a realistic treatment of the Wolf-Rayet (WR) phase, which can result from mergers and envelope removal (D’Agostino et al. 2019). As outlined in Richardson et al. (2019), we adopt a Kroupa initial mass function with exponents 1.3 and 2.35 over the mass ranges $0.1 M_{\odot} < M < 0.5 M_{\odot}$ and $0.5 M_{\odot} < M < 300 M_{\odot}$ with one of three star formation histories (SFHs): an instantaneous burst SFH at age 20 Myr, an instantaneous burst SFH at age 250 Myr, or a continuous SFH at age 250 Myr. For a single stellar population (SSP), 20 Myr corresponds to the age where $[\text{O III}]/\text{H}\beta$ reaches a maximum (Xiao et al. 2018), while 250 Myr corresponds to the age where the ionizing continuum flux for He^{+} and O^{++} ($>54 \text{ eV}$) reaches a maximum. After

⁸ <https://facstaff.elon.edu/crichardson17/>

continuous star formation for 250 Myr, the ionizing continuum ceases to evolve and this provides a stellar SED for “general” use in photoionization modeling. We include 11 different metallicities calibrated to $Z_{\odot} = 0.02$, spanning 0.05–2.0 Z_{\odot} for all SFHs. Figure 3 displays stellar SEDs for each of the three SFHs at 0.4 Z_{\odot} .

To mix the AGN and stellar SEDs, we use both coincident and noncoincident mixing (Figure 1) with AGN fractions ($f_{\text{AGN}} = 0.0, 0.04, 0.08, 0.16, 0.32, 0.5, 0.64, \text{ and } 1.0$, where f_{AGN} represents the fraction of the total ionizing continuum attributed to the AGN SED. Additionally, the cosmic-ray background value $\xi = 2.0 \times 10^{-16} \text{ s}^{-1}$ (Indriolo et al. 2007) is added to satisfy the chemistry network.

2.2. Gaseous Cloud

Following Richardson et al. (2019), we select a hydrogen density of $\log(n_{\text{H}}/\text{cm}^{-3}) = 2.0$ at the illuminated face. After selecting n_{H} , the ionization parameter is then given by

$$U = \frac{\phi_{\text{H}}}{n_{\text{H}}c} \quad (4)$$

where ϕ_{H} is the hydrogen ionizing flux. While most emission line galaxies indicate $\log U$ from -3.5 to -2.0 , an even lower limit is needed to explain the dwarf galaxies with the lowest ionization, and $\log U > -1.5$ is needed to explain local blue compact dwarf galaxies (Stasińska et al. 2015). Accordingly, we run simulations with ionization parameters from $\log U = -4.0$ to $\log U = -0.5$ in increments of $\Delta(\log U) = 0.25$. We follow Abel et al. (2008) by employing a magnetic field and constant-pressure equation of state until all simulations stop at $n_e/n_{\text{H}} = 0.01$. We include a small amount of turbulence ($v = 2 \text{ km s}^{-1}$) to reduce line trapping. We consider both open and closed geometries as given in Figure 1.

We use the methodology in Nicholls et al. (2017) for our abundances and scaling. The solar values for Galactic Concordance abundances are largely based on Nieva & Przybilla (2012), Grevesse et al. (2015), and Scott et al. (2015a, 2015b), which we list in Table 1. The scaling of abundances with metallicity includes a detailed prescription for accounting for specific elemental variations due to differences in nucleosynthesis. Unfortunately, the abundance of oxygen relative to solar has become synonymous with metallicity. While metallicity is strictly defined as the mass fraction of metals, and oxygen makes the greatest contribution to metallicity, the two are not equivalent. To avoid this ambiguity, we refer to the scaling parameter ζ_{O} as the metallicity (see Nicholls et al. 2017) where the solar metallicity is $12 + \log(\text{O}/\text{H}) = 8.76$, corresponding to $\zeta_{\text{O}} = 1$.

We assume Orion grains and PAHs throughout the cloud, as implemented in Baldwin et al. (1991) and Abel et al. (2008), respectively. The dust abundance is typically assumed to not depend on metallicity, while the gas (hydrogen) to dust ratio (G/D) varies as $G/D \propto Z^{-1}$ (Dwek 1998). Here, we adopt a more sophisticated broken power law:

$$\log(G/D) = \begin{cases} 2.21 - \log \frac{Z_{\text{gas}}}{Z_{\odot}} & Z_{\text{gas}} \geq 0.25 Z_{\odot} \\ 0.96 - 3.10 \log \frac{Z_{\text{gas}}}{Z_{\odot}} & Z_{\text{gas}} < 0.25 Z_{\odot}, \end{cases} \quad (5)$$

which shows that low-metallicity dwarfs deviate from a single power-law relation (Rémy-Ruyer et al. 2014). The Orion grain abundances and PAH abundances are scaled from their default

Table 1
Reference Abundances and Depletion Factors δ Used for Included Chemical Elements X

X	$\log(X/\text{H})$	$\delta_X(F_* = 0.45)$
He	−1.01	0.0
Li	−8.722	−0.524
Be	−10.68	−0.274
B	−9.193	−0.546
C	−3.577	−0.120
N	−4.21	0.000
O	−3.24	−0.112
F	−7.56	−0.147
Ne	−3.91	0.0
Na	−5.79	−0.538
Mg	−4.44	−0.659
Al	−5.57	−1.602
Si	−4.50	−0.625
P	−6.59	0.000
S	−4.88	0.0
Cl	−6.75	−0.037
Ar	−5.60	0.0
K	−6.96	−0.614
Ca	−5.68	−2.356
Sc	−8.84	−1.533
Ti	−7.07	−1.928
V	−8.11	−1.159
Cr	−6.38	−1.379
Mn	−6.58	−1.134
Fe	−4.48	−1.510
Co	−7.07	−1.343
Ni	−5.80	−1.517
Cu	−7.82	−0.757
Zn	−7.44	−0.075

Note. We set nonrefractory elements He, Ne, S, and Ar to $\delta_X = 0$. See Appendix A for details.

values by the same factor to satisfy this relationship at a given Z .

Most photoionization modeling assumes a “standard” set of gas-phase depletion factors derived from a variety of sources. In reality, however, depletion factors δ_X depend on the set of undepleted reference abundances being used and the strength of the depletion F_* . We follow a self-consistent approach where we use our unique reference abundances with the methodology outlined in Jenkins (2009). The strength of the depletion is selected so that the depletion factor for iron is $\delta_{\text{Fe}} = -1.5$ dex as in Thomas et al. (2018). This results in $\delta_{\text{O}} = -0.11$ dex, which is less than the commonly assumed Cloudy default of $\delta_{\text{O}} = -0.22$ dex, but assists in matching optical emission line diagnostics (Gutkin et al. 2016) and matches the depletion derived from analyzing dust grain composition (Peimbert & Peimbert 2010), X-ray spectroscopy (Pinto et al. 2013), and α -element enhancement (Amayo et al. 2021). In reality, depletion factors should change with G/D at a fixed metallicity and as a function of metallicity (Peimbert & Peimbert 2010; De Cia et al. 2016); however, this is rarely taken into account in photoionization modeling and is beyond the scope of this work. The complete set of adopted depletion factors are listed in Table 1 and we elaborate on our methodology in Appendix A. Our final gas-phase abundances differ from the BPASS stellar abundances, the effects of which have been investigated in Grasha et al. (2021) but are beyond the scope of this work. All in all, our model suite consists of $\sim 6.33 \times 10^4$ simulations.

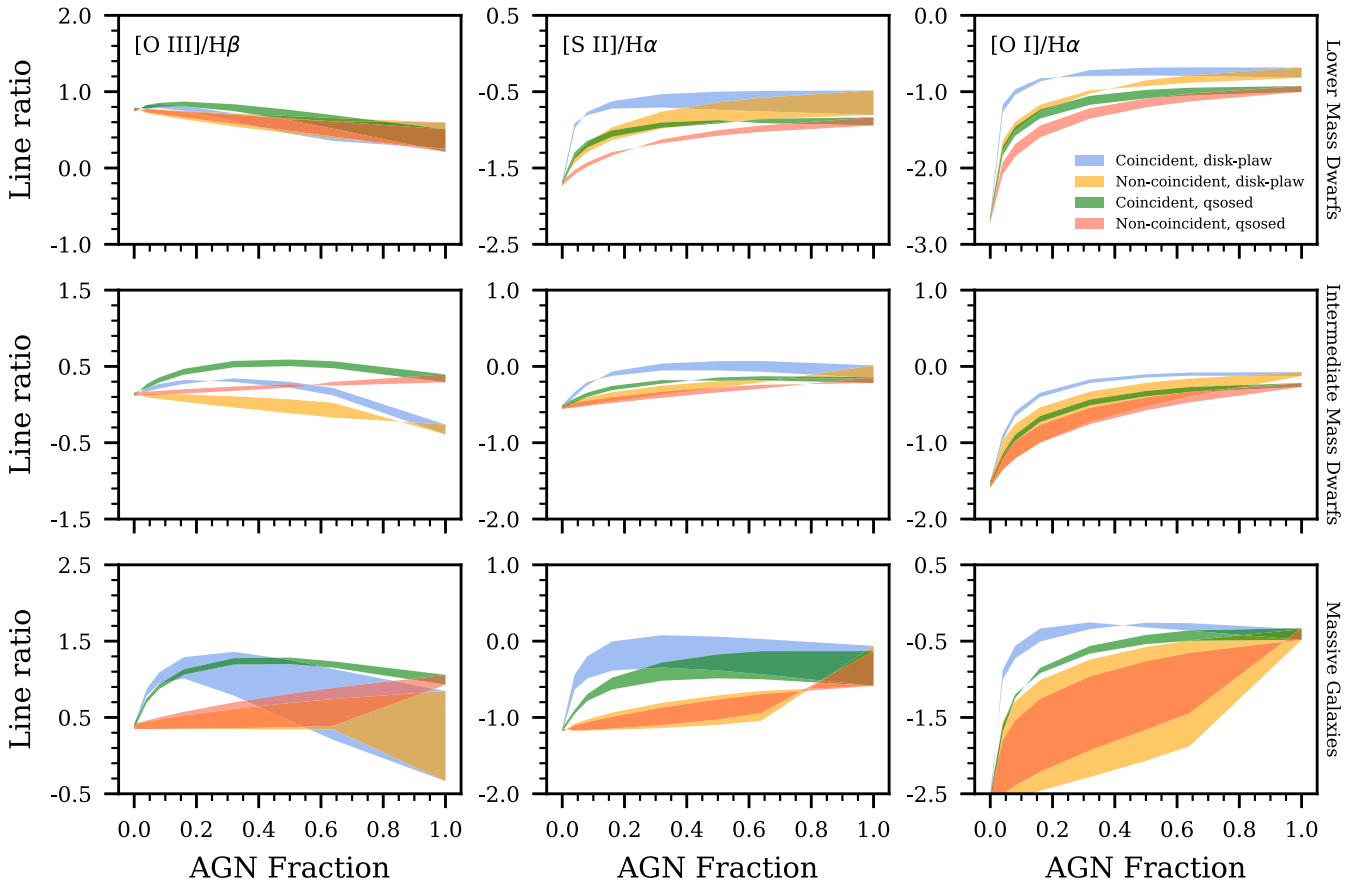


Figure 4. Common optical emission line excitation diagnostics in different galaxy mass regimes (right label) assuming $M_{\text{BH}} = 10^3 M_{\odot}$. The width of the line represents uncertainty due to geometry, while the colors refer to the mixing methodologies from Figure 1 and two SEDs from Figure 2. Each line has been thickened by 0.04 dex for clarity and the y-axis of each panel spans a 3.0 dex range to highlight the relative sensitivity of each emission line to the physical parameters explored.

3. Line Ratio Sensitivity Analysis

We seek to assess the sensitivity of emission line ratios to f_{AGN} , AGN SED shape, mixing methodology, and geometry. In particular, we select emission line diagnostics that are detectable in purely star-forming galaxies, enabling investigation of the connection between star formation and AGN in dwarfs, which is not possible for all emission lines. For example, the presence of [Ne V] $14.3 \mu\text{m}$ or [Ne VI] $7.65 \mu\text{m}$ alone signals AGN activity, but our simulations show that [Ne V] is unlikely to be detectable in most local dwarfs where U and f_{AGN} are small, thus making it an unreliable tracer of AGN fraction for all galaxy masses.

Similarly, coronal lines from highly ionized states (e.g., Si VI, Fe XIII) have been used to identify AGN (Cann et al. 2018; Bohn et al. 2021; Kimbro et al. 2021). However, several limitations exist to this approach: (1) only about half of AGN actually show coronal line(s), regardless of instrumental line sensitivity (Riffel et al. 2006); (2) highly ionized states depend on physical conditions with high $U \sim -2.0$ and high $f_{\text{AGN}} > 0.64$, which are not characteristic of typical dwarfs; (3) if present, the coronal-line region lies between the broad-line and narrow-line regions, which implies dust sublimation is important, a process that presents a problem for self-consistent photoionization modeling (Mazzalay et al. 2010; Adhikari et al. 2016); (4) coronal line emission typically originates from metals that become heavily depleted in forming dust grains (e.g., Si, Ca, Fe), and therefore small changes to F_{\star} yield large differences in these abundances (De Cia et al. 2016). All together, these limitations suggest that

using coronal lines will be subject to strong selection bias, and therefore alone cannot provide a complete picture of IMBH activity in dwarf AGN.

With these caveats in mind, we have determined three different mass ranges to evaluate the AGN emission line diagnostics within the wavelength ranges of the Sloan Digital Sky Survey (SDSS) and JWST: lower-mass dwarfs, intermediate-mass dwarfs, and massive galaxies.

1. For lower-mass dwarfs, we use the U - Z correlation presented in Kashino & Inoue (2019), which leads to values of $\log U \approx -2.0$ and $Z/Z_{\odot} \approx 0.15$.
2. For intermediate-mass dwarfs, we analyzed SDSS strong emission line measurements (Tremonti et al. 2004) as processed by P21 for the $z \sim 0$ dwarf-dominated RESOLVE survey (Kannappan & Wei 2008) with the Bayesian analysis code *NebulaBayes* (Thomas et al. 2018), but using our simulation suite. We determine median values of $\log U \approx -3.25$ and $Z/Z_{\odot} \approx 0.4$ for intermediate-mass dwarfs (P21), which can be thought of as a “fiducial” set of parameters for dwarf galaxies.
3. For massive galaxies, we adopt $\log U \approx -2.0$ and $Z/Z_{\odot} \approx 1.0$ following the parameters used in Abel et al. (2009) to model AGN in massive galaxies such as ULIRGs.

For the rest of Section 3, we use the stellar SED resulting from a continuous SFH at 250 Myr because it represents a “general purpose” ionizing continuum not purposefully constructed for maximizing any particular emission line ratio.

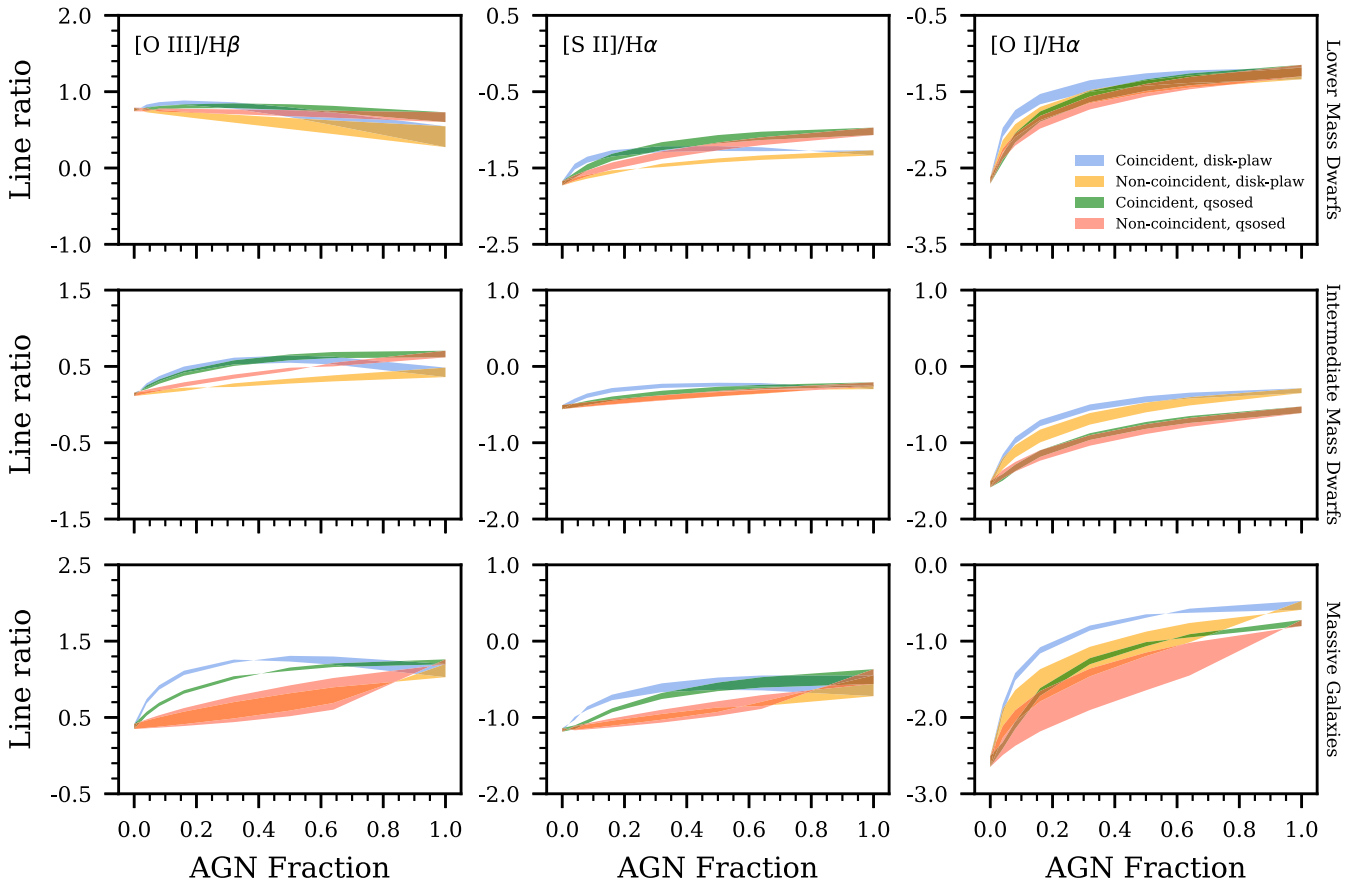


Figure 5. Common optical emission line excitation diagnostics in the same manner as Figure 4 except assuming $M_{\text{BH}} = 10^5 M_{\odot}$.

3.1. Optical

Figures 4 and 5 show the emergent optical emission line predictions for $M_{\text{BH}} = 10^3 M_{\odot}$ and $M_{\text{BH}} = 10^5 M_{\odot}$, respectively. In each figure, we display $[\text{O III}]/\text{H}\beta$, $[\text{S II}]/\text{H}\alpha$, and $[\text{O I}]/\text{H}\alpha$, three common emission line ratios used in optical AGN diagnostics (columns), as a function of AGN fraction for three galaxy mass regimes (rows). The thickness of each line denotes the uncertainty due to differences in assuming a spherical or plane-parallel geometry, while the color indicates the AGN SED and mixing methodology being used. Other diagnostics are presented in Appendix B, such as the metallicity-sensitive $[\text{N II}]/\text{H}\alpha$ ratio.

A few major trends are apparent in Figures 4 and 5. First, the effect that physical uncertainties have on emission line ratios is exacerbated for lower M_{BH} . Second, the greatest variation in emission line ratios due to f_{AGN} occurs in the range $0.0 \leq f_{\text{AGN}} \leq 0.32$. The diagnostics $[\text{O III}]/\text{H}\beta$ and $[\text{S II}]/\text{H}\alpha$ are generally poorer tracers of f_{AGN} . Lastly, in the dwarf galaxy mass regimes, diagnostics show less dependence on geometry, in stark contrast to massive galaxies, where the diagnostics can show up to ~ 1.0 dex variation for $M_{\text{BH}} = 10^3 M_{\odot}$.

The photoionization cross section of hydrogen quickly decreases as photon energy increases (Osterbrock & Ferland 2006). As a result, X-rays due to an AGN penetrate into neutral gas, which causes collisions that excite neutral species. Since $[\text{O I}] \lambda 6300$ partially originates from neutral gas, $[\text{O I}]/\text{H}\alpha$ traces f_{AGN} rather well in dwarf galaxy mass regimes in contrast to the other optical diagnostics. This makes it a reliable choice for detecting AGN activity in dwarfs and constraining f_{AGN} . Non-ionizing photons can also pump electrons into

high-energy excited states, which can cause $[\text{O I}] \lambda 6300$ emission when the electrons cascade to lower energy levels. This continuum fluorescence process is rather inefficient for O I (Bautista 1999), leaving collision excitation as the dominant process, and thus preserving the utility of $[\text{O I}] \lambda 6300$ as an AGN diagnostic.

The AGN SED and mixing methodology can create substantial variation in all diagnostics, although this is mitigated for emission line ratios created under certain physical conditions. For example, the middle rows of Figures 4 and 5 show that considering $f_{\text{AGN}} \geq 0.32$, the emission line ratios converge upon $[\text{O III}]/\text{H}\beta \approx -0.3$ to 0.7 and $[\text{O I}]/\text{H}\alpha \approx -1.2$ to -0.2 , generally resulting in a LINER classification (Kewley et al. 2006). This result, combined with a star-forming galaxy classification from the metallicity-sensitive BPT diagram, corroborates that dwarf AGN have inconsistent optical classifications (Reines et al. 2020, P21) for black hole masses in the range 10^3 – $10^5 M_{\odot}$.

Our results also stand in contrast to other work (Cann et al. 2019), suggesting that AGN host galaxies with $\sim 10^3 M_{\odot}$ BHs have such low $[\text{O III}]/\text{H}\beta \approx -1.5$ that $[\text{O III}]$ emission might be undetectable.⁹ Figure 4 clearly shows that $[\text{O III}]/\text{H}\beta$ is highly dependent on the physical uncertainties presented in Figure 1 and the galaxy mass regime of interest. RESOLVE dwarf galaxies are ubiquitously star-forming with $f_{\text{AGN}} < 0.6$ and are the most likely hosts for IMBHs. For the intermediate-mass

⁹ Private communication with Jenna Cann, Shobita Satyapal, and Nick Abel suggests that possible physical explanations could include differences in assumed AGN SED shape, in choice of elemental abundances, or in geometry and mixing, as diagrammed in Figure 1.

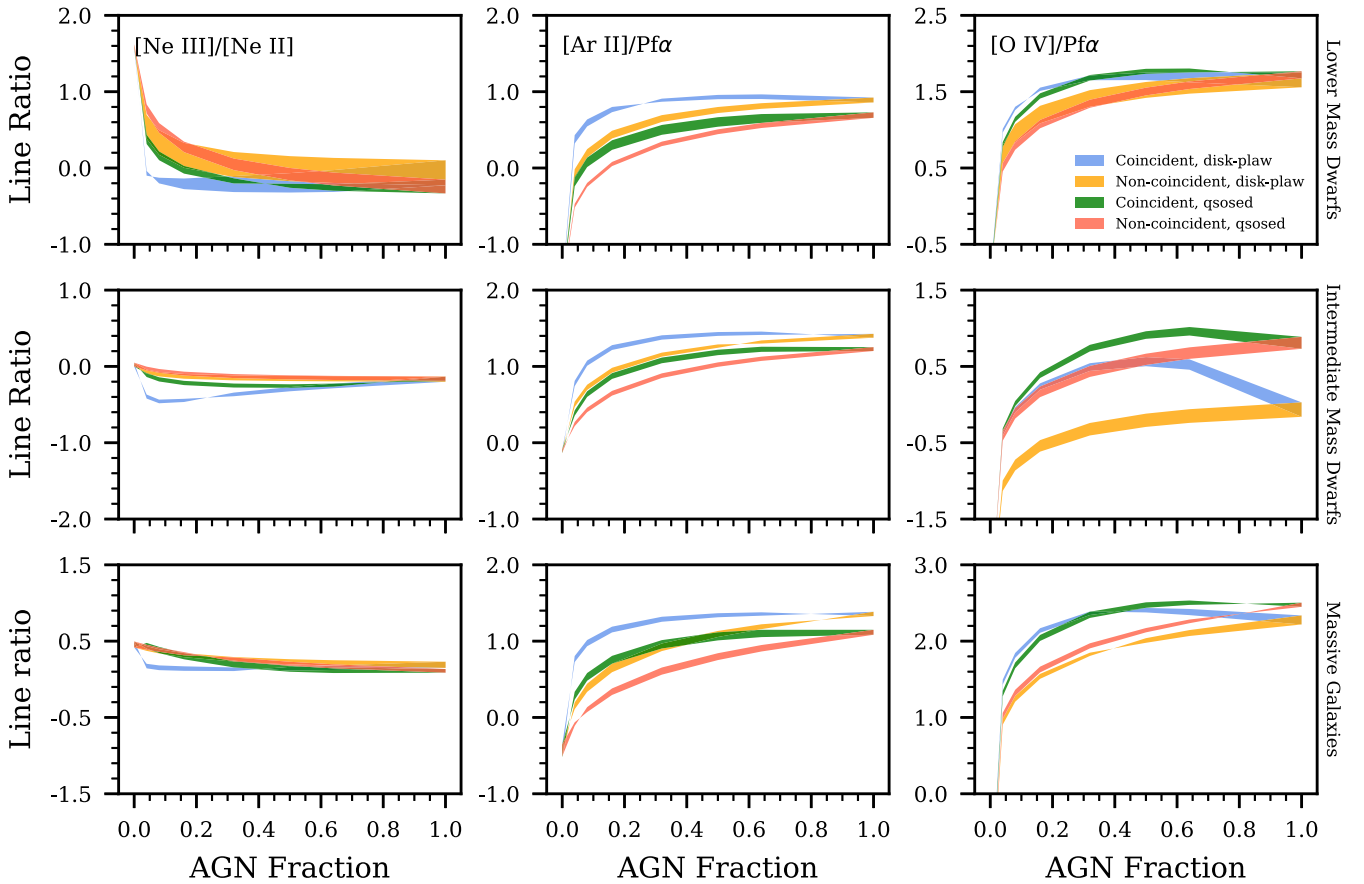


Figure 6. AGN diagnostics with the JWST MIRI instrument in the same format as Figure 4 assuming $M_{\text{BH}} = 10^3 M_{\odot}$.

dwarf galaxy regime, we see in the majority of cases that $[\text{O III}]/\text{H}\beta \geq 0.0$, i.e., $[\text{O III}]$ is as strong as $\text{H}\beta$.

3.2. Mid-IR

The most valuable AGN diagnostics for JWST come from the MIRI instrument (4.9–28.3 μm), as opposed to NIRspec (0.6–5.3 μm), based on the availability of either emission lines originating from the same element with different ionization potentials, or high ionization lines along with a recombination line for comparison. Although we are focused on detecting active IMBHs in relatively local galaxies, it is worth noting that galaxies at $z > 0.3$ will have optical diagnostics that fall within NIRspec, thereby providing additional constraints. The following lines show diagnostic value for AGN activity and are detectable until $z \sim 0.1$ assuming the MIRI line sensitivity of $3.3 \times 10^{-17} \text{ erg s}^{-1} \text{ cm}^{-2}$: $\text{Pf}\alpha$, $[\text{Ne II}]$ 12.8 μm , $[\text{Ne III}]$ 15.6 μm , $[\text{Ar II}]$ 6.98 μm , $[\text{Ar III}]$ 8.99 μm , $[\text{Ar V}]$ 13.1 μm , $[\text{S III}]$ 18.7 μm , $[\text{S IV}]$ 10.5 μm , and $[\text{O IV}]$ 25.9 μm . This result is independent of geometry, mixing methodology, or AGN SED shape.

Figures 6 and 7 display tracers of AGN activity observable with JWST, in the same format as Figures 4 and 5. As in the optical, changes to the line ratios become less pronounced as AGN fraction increases; in contrast to the optical, IR line ratios generally show less sensitivity to geometry. Weaver et al. (2010) suggests that $[\text{Ne III}]/[\text{Ne II}]$ and $[\text{O IV}]/[\text{Ne III}]$ have the ability to effectively separate excitation mechanisms. The first column in both figures indicates that $[\text{Ne III}]/[\text{Ne II}]$ remains constant with AGN fraction for intermediate-mass dwarfs (second row) and massive galaxies (third row).

Therefore, $[\text{Ne III}]/[\text{Ne II}]$ is not a robust indicator of AGN activity. It does, however, remain an effective f_{AGN} diagnostic for the low-mass dwarf galaxies, with minor sensitivity to the mixing methodology and SED selection. The second column shows that $[\text{Ar II}]/\text{Pf}\alpha$ has strong diagnostic potential for all galaxy masses, especially for $M_{\text{BH}} = 10^5 M_{\odot}$ (Figure 7). As M_{BH} decreases, $[\text{Ar II}]/\text{Pf}\alpha$ still effectively traces f_{AGN} , but the uncertainty of the AGN SED and mixing methodology introduces greater spread in the emission line predictions.

The last column in Figures 6 and 7 shows that $[\text{O IV}]/\text{Pf}\alpha$ is also an effective f_{AGN} diagnostic. At $M_{\text{BH}} = 10^5 M_{\odot}$, $[\text{O IV}]/\text{Pf}\alpha$ traces f_{AGN} quite well, while remaining relatively insensitive to the shape of the AGN SED and the uncertainties given in Figure 1. $[\text{O IV}]/\text{Pf}\alpha$ remains well-behaved for $M_{\text{BH}} = 10^3 M_{\odot}$ except for intermediate-mass dwarfs, where the disk-plaw, noncoincident mixing case creates a ~ 1.0 dex spread in values relative to the other cases. This spread is due to the combined effect of a low U and harder accretion disk reducing the number O^{++} ionizing photons.

In general, line ratios featuring $[\text{O IV}]$ and $[\text{Ar II}]$ show less sensitivity to geometry than optical diagnostics, display more variation with AGN fraction than other mid-IR line ratios, and retain their diagnostic potential over a wider range of galaxy masses and BH masses. The mid-IR diagnostics provide greater constraints on f_{AGN} for lower levels of AGN activity expected for dwarf AGN compared to optical diagnostics, which are more sensitive to higher levels of AGN activity. These results highlight the benefit of using multiple line ratios to constrain f_{AGN} with diagnostic diagrams.

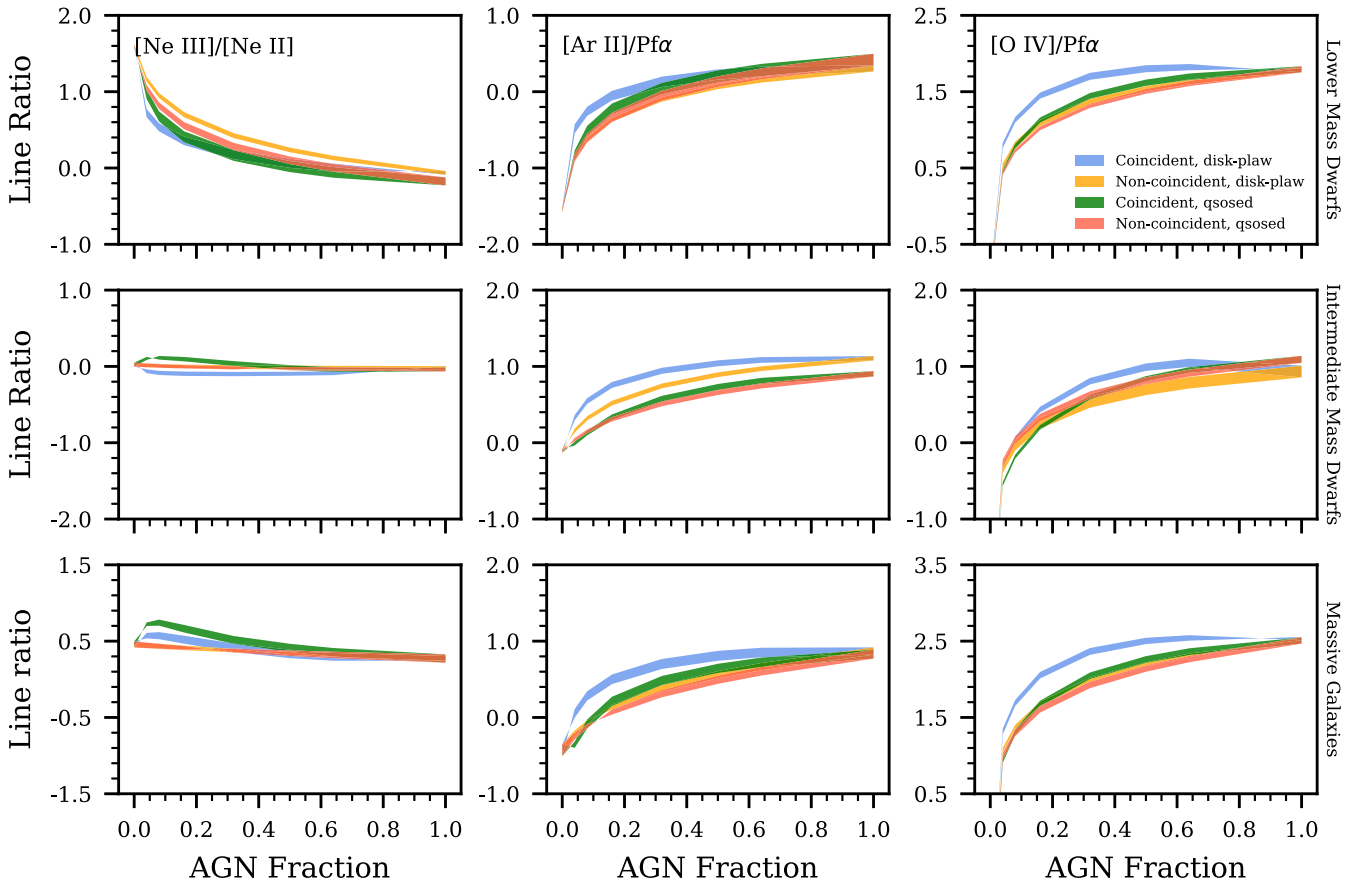


Figure 7. AGN diagnostics with the JWST MIRI instrument in the same format as Figure 5 assuming $M_{\text{BH}} = 10^5 M_{\odot}$.

4. Diagnostics Diagrams

In light of the wide range of uncertainties previously mentioned, we seek to find diagnostic diagrams suitable for detecting AGN excitation, and ideally measuring f_{AGN} , for a given galaxy. To compare our models to galaxies with spectroscopic observations, we select a subset of models ($-3.5 \leq \log U \leq -1.5$) with an instantaneous SFH, since the harder stellar continua provide a limiting case for AGN activity.

4.1. Optical

We use a 20 Myr SSP for the optical diagnostics since this SFH maximizes the $[\text{O III}]/\text{H}\beta$ line ratio used in many diagnostic diagrams that separate AGN and star-forming galaxies. For the observational sample, we choose dwarf galaxies in the MPA-JHU sample from P21. Following P21, we classify dwarf AGN as any dwarf galaxies not classified as definitely star-forming (e.g., traditional AGN, LINERs, etc.) The three diagrams from Veilleux & Osterbrock (1987) are by far the most commonly used optical diagnostics for separating AGN and star-forming galaxies, so we focus our analysis on them.

Figure 8 displays these diagrams for $M_{\text{BH}} = 10^3 M_{\odot}$ (left column) and $M_{\text{BH}} = 10^5 M_{\odot}$ (right column). The models for $f_{\text{AGN}} = 0.04$, $f_{\text{AGN}} = 0.08$, and $f_{\text{AGN}} \geq 0.16$ approximately span the area of the three hatched shapes (tan, purple, and green, respectively). For models with $f_{\text{AGN}} \geq 0.16$ and a $10^3 M_{\odot}$ black hole, there is a wide range of possible values for $[\text{O III}]/\text{H}\beta$, highly dependent on configurations present in Figure 1. This large spread in values relates to the current difficulty of

detecting IMBHs at this mass, but also provides promise that optical detection is indeed possible.

Figure 8 shows that models in the range $0 \leq f_{\text{AGN}} \leq 0.16$ occupy similar regions of each diagram. In particular, the BPT diagram (top row) registers observed dwarf AGN as consistent with pure star formation. Conversely, theoretical models with pure star formation can cross over into the AGN region of the diagram. Despite the differences in photoionization modeling, this is also seen in Xiao et al. (2018) on account of using the BPASS SEDs that feature substantially harder continua than many other SPS codes.

The $[\text{S II}]/\text{H}\alpha$ diagram indicates that pure star formation can reproduce the line ratios of all the dwarf AGN shown, but in this diagram, unlike for the BPT diagram, this result only occurs with the particularly hard stellar SED that we have selected. Thus, knowing the SFHs for a given sample of dwarfs could provide justification for using $[\text{S II}]/\text{H}\alpha$ to identify AGN. In contrast, the BPT diagram is more generally a poor diagnostic for identifying dwarf AGN, regardless of SFH, as discussed in more detail in P21.

The last optical diagnostic diagram shows that some dwarf AGN require models with an AGN component to reproduce the observed $[\text{O I}]/\text{H}\alpha$, making this diagram more reliable in separating star formation and AGN in dwarfs (Reines et al. 2020, P21). It is worth noting that more dwarf AGN likely require an AGN component than shown here, on account of the hard stellar SED used in this analysis. Additionally, for $[\text{O I}]/\text{H}\alpha$ there is some modest separation between models with different f_{AGN} , especially with $M_{\text{BH}} = 10^3 M_{\odot}$, enabling a better assessment of AGN activity as also shown in Figure 4.

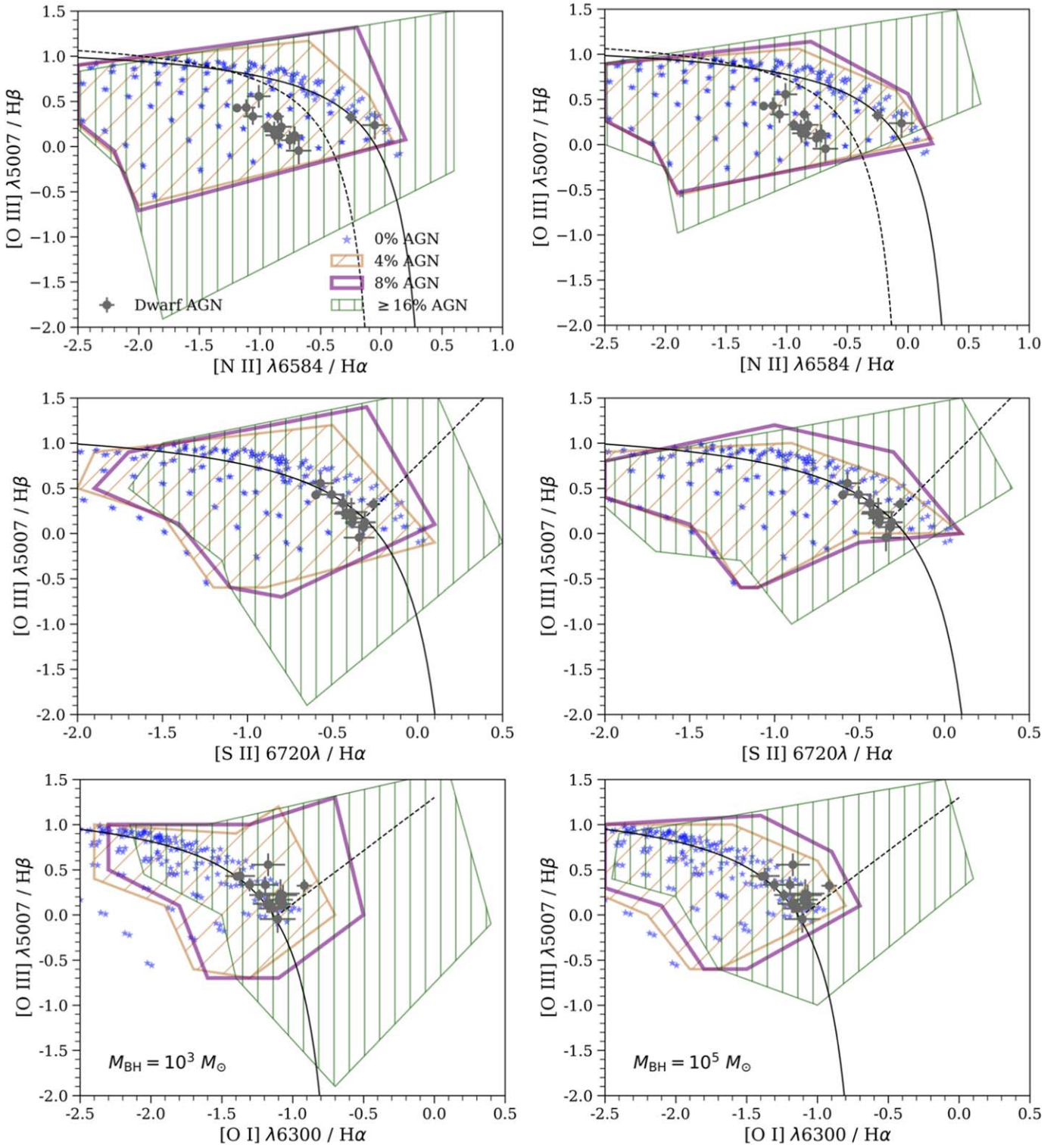


Figure 8. Optical diagnostic diagrams that separate AGN activity from starburst activity assuming $M_{\text{BH}} = 10^3 M_{\odot}$ (left column) and $M_{\text{BH}} = 10^5 M_{\odot}$ (right column). The selected age of the binary stellar population maximizes the contribution of WR stars and thereby sets a lower limit for AGN activity. Pure starburst models (0% AGN) are displayed as blue stars. The models for a given f_{AGN} approximately span the area of each hatched shape. The demarcations in each diagram are taken from Kewley et al. (2001, 2006) and Kauffmann et al. (2003). The majority of observed dwarf AGN lie in the star-forming wing of the BPT diagram (top panels), which models with and without AGN can reproduce.

4.2. Mid-IR

For our observational sample, we choose dwarf SF (Cormier et al. 2015) and dwarf AGN (Hood et al. 2017) observations requiring that the latter satisfy $[\text{Ne V}]/[\text{Ne II}] > 0.1$ (Inami et al. 2013). It is important to note that $\text{P}\alpha$, featured in

Figure 6, is not available in statistical samples due to the low sensitivity and resolution of Spitzer and the Infrared Space Observatory. Similarly, since $[\text{Ar II}] 6.98 \mu\text{m}$ is unavailable for samples including dwarfs, we use massive AGN (Sturm et al. 2002) for diagnostic diagrams with this line.

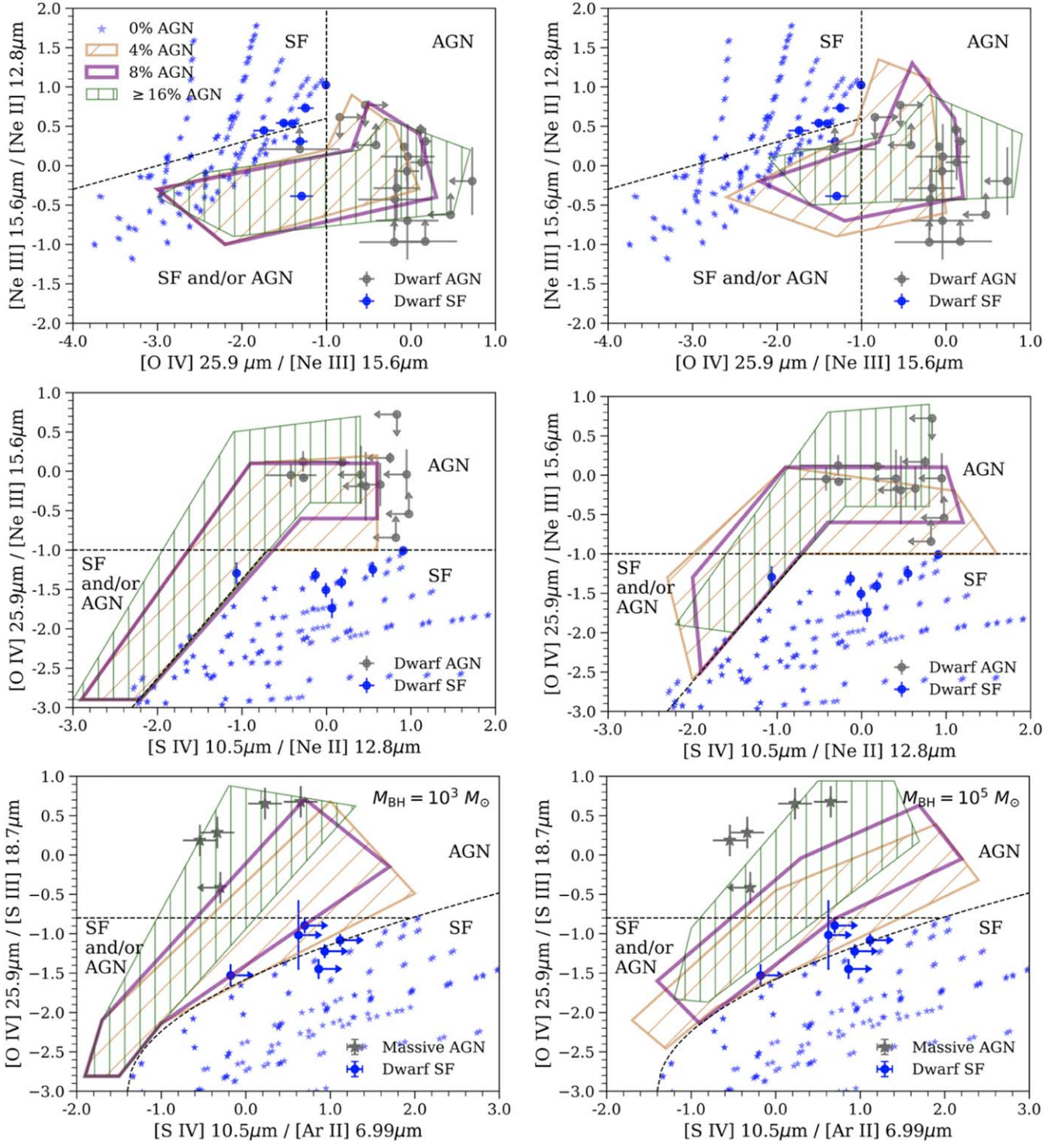


Figure 9. Mid-IR diagnostic diagrams that separate AGN activity from pure starburst activity in the same format as Figure 8. Pure starburst models (0% AGN) are displayed as blue stars. The models for a given f_{AGN} approximately span the area of each hatched shape. The regions SF, SF and/or AGN, and AGN represent pure starburst galaxies, a mix of pure starburst galaxies and AGN, and only AGN, respectively (Equations (6)–(8)). JWST will enable emission lines normally missing from Spitzer spectra to serve as additional constraints, like [Ar II] 6.99 μm (left panels).

We have tested all possible combinations of emission line ratios from the emission lines listed in Section 3.2. Figure 9 shows the results of this analysis in three diagnostic diagrams featuring emission line ratios also presented in Weaver et al. (2010), Inami et al. (2013), and Hao et al. (2009).

Our new demarcations separate three distinct regions: the SF region contains only pure starburst galaxies; the SF and/or

AGN region contains a mixture of pure starbursts and AGN; the AGN region contains only AGN. The divisions between SF and SF and/or AGN regions are given by

$$\log([\text{Ne III}]/[\text{Ne II}]) = 0.3 \log([\text{O IV}]/[\text{Ne III}]) - 0.9 \quad (6)$$

$$\log([\text{O IV}]/[\text{Ne III}]) = 1.25 \log([\text{S IV}]/[\text{Ne II}]) - 0.125 \quad (7)$$

$$\log([\text{O IV}]/[\text{S III}]) = 1.2 (\log([\text{S IV}]/[\text{Ar II}]) + 1.4^{1/2} - 3.0) \quad (8)$$

while the AGN region is formed by $[\text{O IV}]/[\text{Ne III}] = -1$ and $[\text{O IV}]/[\text{S III}] = -0.8$.

The first diagram (top panels) has frequently been used to separate starbursts and AGN into quadrants according to $[\text{O IV}]/[\text{Ne III}] = 0$ (Weaver et al. 2010), but this cutoff excludes dwarf AGN with $[\text{O IV}]/[\text{Ne III}] > -1$, which our new demarcations recover. Our models indicate that the observed dwarf AGN in this region have at least a 4%–16% AGN contribution. The second diagram (center panels) replaces the abscissa with $[\text{S IV}]/[\text{Ne II}]$ (Inami et al. 2013), resulting in a cleaner separation of starbursts and AGN at low ionization. The last diagram (bottom panels) uses $[\text{O IV}]/[\text{S III}]$ in the ordinate (Hao et al. 2009) and $[\text{S IV}]/[\text{Ar II}]$ in the abscissa, which creates even more separation between starbursts and AGN, and also between f_{AGN} values. As mentioned above, the $[\text{Ar II}]$ observations are poor since Spitzer was only capable of detecting wavelengths $< 10 \mu\text{m}$ in low-resolution mode ($R \sim 130$). In contrast, MIRI features the highest resolution ($R \sim 3100$) and line sensitivity available at these wavelengths. Thus, the right panels in Figure 9 present a promising new diagnostic for JWST observations to constrain AGN activity.

5. Discussion and Conclusions

In this paper, we have explored several key uncertainties that will be critical to assess in the upcoming era of detecting IMBHs: the shape of the AGN SED, the geometry of the surrounding gas cloud, and the manner of mixing radiation from AGN and stars. The diversity of models for the AGN SED in Figure 2 emphasizes the importance of next-generation X-ray facilities such as Lynx and Athena that will enable proper constraints on low-luminosity sources. We show that all of the listed uncertainties have profound effects on emission line diagnostics in the optical and mid-IR. This has implications for statistical samples of galaxies that are analyzed with photoionization models that implicitly assume a particular geometrical configuration or mixing methodology in Figure 1. Such assumptions can lead to powerful selection effects (Ferguson et al. 1997; Meskhidze & Richardson 2017). These assumptions could limit the applicability of simple relationships that scale physical properties (e.g., f_{AGN} , M_{BH}) with emission line ratios for large samples of galaxies.

Even though degeneracies abound in the optical, we find AGN diagnostics remain detectable in most situations across a range of galaxy masses. This result offers promise that surveys like SDSS have already picked up signatures of AGN with $M_{\text{BH}} = 10^3 M_{\odot}$. Unfortunately, the gold standard for optical AGN classification, the BPT diagram, poorly traces AGN activity in dwarf galaxies. As we argue in P21, this is due to $[\text{N II}]/\text{H}\alpha$ being metallicity-sensitive and f_{AGN} insensitive. It also reflects the sensitivity of $[\text{O III}]/\text{H}\beta$ to the uncertainties explored in this paper. Actually, as seen in Reines et al. (2020) and P21, the often forgotten $[\text{O I}]/\text{H}\alpha$ diagnostic is a stronger metric for an active AGN in dwarfs given its sensitivity to f_{AGN} and relative insensitivity to physical uncertainties. It therefore serves as the best optical emission line ratio for finding dwarf AGN, but the relative weakness of the $[\text{O I}]$ line does limit the sample that can be tested (P21).

Relatively high-mass dwarfs ($M_* \lesssim 10^{9.3-9.5} M_{\odot}$) classified as LINERs present an opportunity to find the coveted $10^3 M_{\odot}$

black holes, which would fill in a major gap in IMBH empirical relationships and help constrain the occupation fraction in dwarfs. If AGN in this BH mass regime are confirmed by other methods (e.g., variability, line broadening, X-rays), but still fail to show any optical signatures, this nondetection would suggest that the column density of obscuring gas and the covering factor around the source could be factors in the elusive nature of these AGN. The column densities and covering factors of dwarf AGN remain relatively unexplored. Purely star-forming dwarf galaxies show a decrease in covering factor as metallicity decreases, albeit with a large scatter in the relation (Cormier et al. 2019). Conversely, massive galaxies show a decrease in obscured AGN (large covering factor) with increasing luminosity (Sazonov et al. 2015; Georgakakis et al. 2017) and therefore increasing metallicity (Lamareille et al. 2004). It is possible that dwarf AGN could provide the missing link between these two opposing trends if low-mass IMBHs continue to remain elusive in the optical.

In the mid-IR, we have shown that $[\text{Ar II}] 6.98 \mu\text{m}/\text{Pf}\alpha$ and $[\text{O IV}] 25.9 \mu\text{m}/\text{Pf}\alpha$ together have the potential to constrain AGN activity over a range of galaxy masses while minimizing sensitivity to physical uncertainties (Figure 6). We have revised the demarcations on the $[\text{Ne III}]/[\text{Ne II}]$ versus $[\text{O IV}]/[\text{Ne III}]$ diagnostic diagram to include dwarf AGN and presented two new diagnostic diagrams based on the $[\text{O IV}]$ and $[\text{Ar II}]$ emission lines (Figure 9). These new diagrams are capable of separating starburst activity from AGN activity down to a 4% AGN fraction in dwarfs, which are ubiquitously star-forming. Unlike the BPT diagram, these proposed diagrams maintain their diagnostic value over a wide range of ionization and metallicity.

We emphasize that the demarcations provided serve as theoretical boundaries for classifying the excitation mechanism in dwarf galaxies. Observations of optically classified starbursts can occasionally cross over into the AGN region of these diagrams due to strong mid-IR $[\text{O IV}]$ emission (e.g., IZw18, Lebouteller et al. 2017), although soft X-ray and hard X-ray emission is typically detected in these galaxies.

Current SPS models are unable to produce enough photons $> 54 \text{ eV}$ to account for this crossover. High-mass X-ray binaries (HMXBs) can generate the hard photons needed to create AGN-like emission line ratios assuming a model with high U , high L_X/SFR , and a sufficiently hard SED (Simmonds et al. 2021). It is unlikely that HMXBs can uniformly account for dwarfs exhibiting emission line ratios characteristic of AGN given that the shape of the HMXB SED remains highly uncertain and most dwarf AGN do not present these extreme conditions (P21). Additionally, a more generic treatment of the HMXB SED has shown that HMXBs are an inefficient means of producing photons $> 54 \text{ eV}$ (Senchyna et al. 2020). Therefore, unless more realistic treatment of the WR phase alters the result of our predictions in the future, our current simulations suggest these galaxies have active AGN. The SF and/or AGN region in each diagram can contain optically classified starbursts (see Figure 9), and this result is reproduced by a photoionization model with multiple gas clouds (Meléndez et al. 2014; Richardson et al. 2016). Integral field unit observations should help clarify whether such a model needs to be invoked.

To fully address modeling degeneracies in both the optical and mid-IR, Bayesian analysis will be a valuable tool for extracting meaningful properties over a range of conditions in future studies. Our simulation suite incorporates a finer spacing of metallicities, ideal for accurate Bayesian analysis at $< 0.4 Z_{\odot}$

(Richardson et al. 2019), than other SPS models (e.g., Starburst99), while robustly accounting for G/D and elemental depletion. In addition, the mixing methodologies and geometries unique to our models could be used in a multicomponent analysis of the interstellar medium (ISM), similar to work on the multiphase ISM in dwarfs (Cormier et al. 2019). Together with the AGN diagnostics and excitation diagrams presented in this paper, such future applications of our models will prove useful for addressing more complex topologies associated with mixed AGN/SF excitation in dwarfs in the era of JWST.

C.R. gratefully acknowledges the support of the Elon University FR&D committee and the Extreme Science and Engineering Discovery Environment (XSEDE), which is supported by National Science Foundation grant no ACI-1548562. This work used the XSEDE resource Comet at the San Diego Supercomputing Center through allocation TG-AST140040. M.P. gratefully acknowledges the support of the 2020 Hamilton Award from the UNC Department of Physics and Astronomy. S.K. and M.P. acknowledge support from NSF AST-2007351. J.B. acknowledges grant support from NSF AST-1812642 and CUNY JFRASE. We thank Nick Abel, Jenna Cann, Chris Done, Gary Ferland, Ed Jenkins, and Shobita Satyapal for helpful discussions that improved the quality of this paper.

Software: Cloudy (Ferland et al. 2017), NebulaBayes (Thomas et al. 2018).

Appendix A Depletion Factors Due to Grains

We use the methodology presented in Jenkins (2009, hereafter J09) to develop a set of depletion factors that account for gas-phase elements condensing to form dust grains. This depletion depends on comparing set of a reference abundances to abundances derived from observations along a particular line of sight. The difference provides the depletion factor, δ_X :

$$\delta_X = \log\left(\frac{X}{H}\right)_{\text{obs}} - \log\left(\frac{X}{H}\right)_{\text{ref}}. \quad (\text{A1})$$

Despite the dependence on a set of reference abundances, most photoionization modeling does not properly take this factor into account, as shown below. Different lines of sight yield different depletion factors for a given element, allowing one to define a depletion strength, F_* , that accounts for this variation. A linear fit to the logarithm of the depletion factor gives the following form:

$$\delta_X = B_X + A_X(F_* - z_X) \quad (\text{A2})$$

where A_X is the slope, B_X is the vertical offset, and z_X accounts for the errors in the observations. We assume that the nonrefractory elements He, Ne, S, and Ar do not become depleted in the ISM. However, sulphur depletion remains a subject of debate (Gry & Jenkins 2017; Laas & Caselli 2019; Goicoechea & Cuadrado 2021; Hily-Blant et al. 2021).

We use the fits for the Galaxy provided in J09 for C, N, O, Mg, Si, P, Cl, Ti, Cr, Mn, Fe, Ni, Cu, and Zn. We make this choice for two reasons. First, J09 provides the most complete sample, while extragalactic fits are mostly limited to heavier elements that have less impact on emission line predictions. Second, the number of observations included in the J09 analysis makes the fit more reliable.

While we assume that depletion occurs as observed in the Milky Way, deviations in the depletion patterns for heavy

Table 2
Depletion Factors Adjusted for Our Set of Reference Abundances at $F_* = 1.0$ along with the Parameters Necessary to Scale Each Element with F_*

X	$\delta_X(F_* = 1.0)$	A_X	B_X	z_X	Ref.
He	0.0	—	—	—	—
Li	-0.827	-0.552	-0.28	—	White (1986)
Be	-0.432	-0.288	-0.14	—	York et al. (1982)
B	-0.862	-0.575	-0.29	—	Federman et al. (1993)
C	-0.176	-0.101	-0.16	0.803	Jenkins (2009)
N	0.000	0.0	0.0	0.550	Jenkins (2009)
O	-0.235	-0.225	-0.15	0.598	Jenkins (2009)
F	-0.470	-0.587	0.117	—	Snow et al. (2007)
Ne	0.0	—	—	—	—
Na	-0.850	-0.567	-0.283	—	Savage & Sembach (1996)
Mg	-1.208	-0.997	-0.74	0.531	Jenkins (2009)
Al	-2.530	-1.687	-0.843	—	Barker et al. (1984)
Si	-1.250	-1.136	-0.46	0.305	Jenkins (2009)
P	-0.520	-0.945	-0.04	0.488	Jenkins (2009)
S	0.0	—	—	—	—
Cl	-0.720	-1.242	-0.23	0.609	Jenkins (2009)
Ar	0.0	—	—	—	—
K	-0.970	-0.647	-0.323	—	Chaffee & White (1982)
Ca	-3.720	-2.480	-1.24	—	Crinklaw et al. (1994)
Sc	-2.421	-1.614	-0.807	—	Snow & Dodgen (1980)
Ti	-3.054	-2.048	-1.89	0.43	Jenkins (2009)
V	-1.830	-1.220	-0.61	—	Savage & Sembach (1996)
Cr	-2.175	-1.447	-1.41	0.47	Jenkins (2009)
Mn	-1.605	-0.857	-1.19	0.52	Jenkins (2009)
Fe	-2.216	-1.285	-1.49	0.437	Jenkins (2009)
Co	-2.120	-1.413	-0.707	—	Mullman et al. (1998)
Ni	-2.336	-1.49	-1.74	0.599	Jenkins (2009)
Cu	-1.147	-0.71	-0.94	0.711	Jenkins (2009)
Zn	-0.410	-0.61	-0.14	0.555	Jenkins (2009)

Note. The nonrefractory elements He, Ne, S, and Ar are assumed to have no depletion.

elements are known to be present for other galaxies. For example, Mg, Ti, and Mn show noticeable deviations in the Small Magellanic Cloud (Jenkins & Wallerstein 2017), and while the depletion pattern is mostly Galactic in the Large Magellanic Cloud (Tchernyshyov et al. 2015), Si does show a noticeable deviation (Roman-Duval et al. 2019).

For the rest of the elements, we have compiled a list of depletion factors toward the highly depleted star ζ Oph to serve as the value at $F_* = 1.0$ in accordance with the method used by J09. Fluorine is the only exception, where we use the most depleted source in Snow et al. (2007), since the value toward ζ Oph is unavailable. To determine the parameters A_X and B_X for these elements, we rely on the general trend that elements with higher condensation temperatures show greater depletions and steeper slopes. The following elements have similar depletion trends to their J09 counterparts: Li \Leftrightarrow Cr; Be \Leftrightarrow Mg; B \Leftrightarrow Zn, F \Leftrightarrow Cl; Na, K \Leftrightarrow Cu, Zn; Al, Ca, V \Leftrightarrow Ti; Sc \Leftrightarrow P, Cu; Co \Leftrightarrow Ni. From these analogies, we can assume that all of the elements in J09 have $\delta_X = 0$ at $F_* \approx -0.5$ except for δ_{Fluorine} , which reaches zero at $F_* = 0.2$.

Table 2 lists the depletion factors for all elements for $F_* = 1.0$, the linear fit parameters needed to recreate the depletion pattern, and the reference for each depletion factor

given. Note that depletion factors have been rescaled according to our reference abundances instead of using the abundance assumed in each cited source. Displaying the depletion factors for $F_* = 1.0$ makes it clear which elements are weakly depleted in the ISM as opposed to not depleted at all. However, for our photoionization modeling, we adjusted F_* so that $\delta_{\text{Fe}} = -1.5$ (see Table 1), which we justified in Section 2.2.

The methodology we have used here is similar to what resulted in the sets of depletion factors included with the photoionization code `Mappings V` (Sutherland & Dopita 2017) with two major differences. First, unlike the values included with `Mappings`, our depletion factors are self-consistently scaled with our reference abundances. Second, we do not deplete nitrogen for any value of F_* given the lack of evidence that nitrogen gets locked up in grains. This is particularly important for any analysis that strongly relies upon nitrogen emission lines for inferring metallicity values.

The depletion factors we use represent a small step toward accounting for the different depletion patterns in gas-phase abundances, much in the same way that Nicholls et al. (2017) accounts for nucleosynthesis patterns for elements as a function of metallicity. However, obvious limitations exist since galaxies can show more negative F_* than we account for here (Jenkins & Wallerstein 2017).

Appendix B Additional Line Ratio Sensitivity Diagrams

In this appendix, we present the line ratio sensitivity for additional AGN diagnostics. Figures 10 and 11 display diagnostics in the optical for $M_{\text{BH}} = 10^3 M_{\odot}$ and $M_{\text{BH}} = 10^5 M_{\odot}$, respectively, and similarly in the mid-IR for Figures 12 and 13. The columns of each figure represent a given galaxy mass, while the rows represent a given line ratio. As with the diagnostics presented in the main body of the paper, the uncertainty introduced from the shape of the AGN SED, cloud geometry, and mixing methodology decreases at higher black hole mass.

In the optical, most of the emission line ratios poorly trace f_{AGN} . It is noteworthy that $[\text{N II}]/\text{H}\alpha$ remains relatively insensitive to AGN activity in most conditions, which combined with the line ratio's sensitivity to metallicity makes it an overall poor diagnostic for dwarf AGN. In contrast, $\text{He II}/\text{H}\beta$ and $[\text{O I}]/[\text{O III}]$ are promising diagnostics for dwarf AGN. However, the wind from WR stars can contaminate He II (Brinchmann et al. 2008), therefore line ratios involving $[\text{O I}]$ are more reliable.

In the mid-IR, one also needs to be judicious in selecting AGN-sensitive diagnostics. For a $10^3 M_{\odot}$ black hole, $[\text{Ar V}]/\text{P}\alpha$, $[\text{Ar V}]/[\text{Ar III}]$, and $[\text{O IV}]/[\text{Ne II}]$ suffer from large

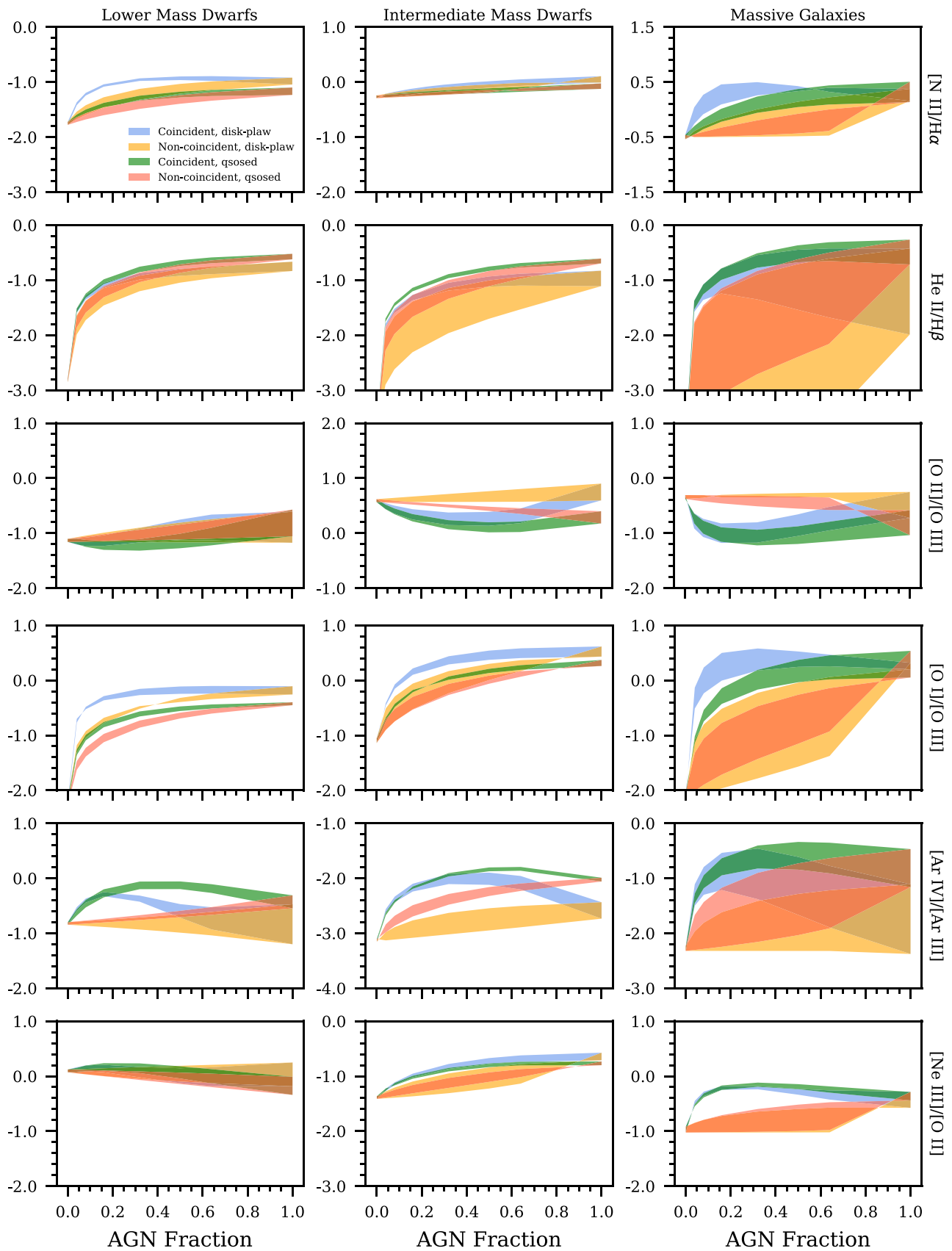


Figure 10. Additional optical emission line excitation diagnostics in the same format as Figure 4 with $M_{\text{BH}} = 10^3 M_{\odot}$.

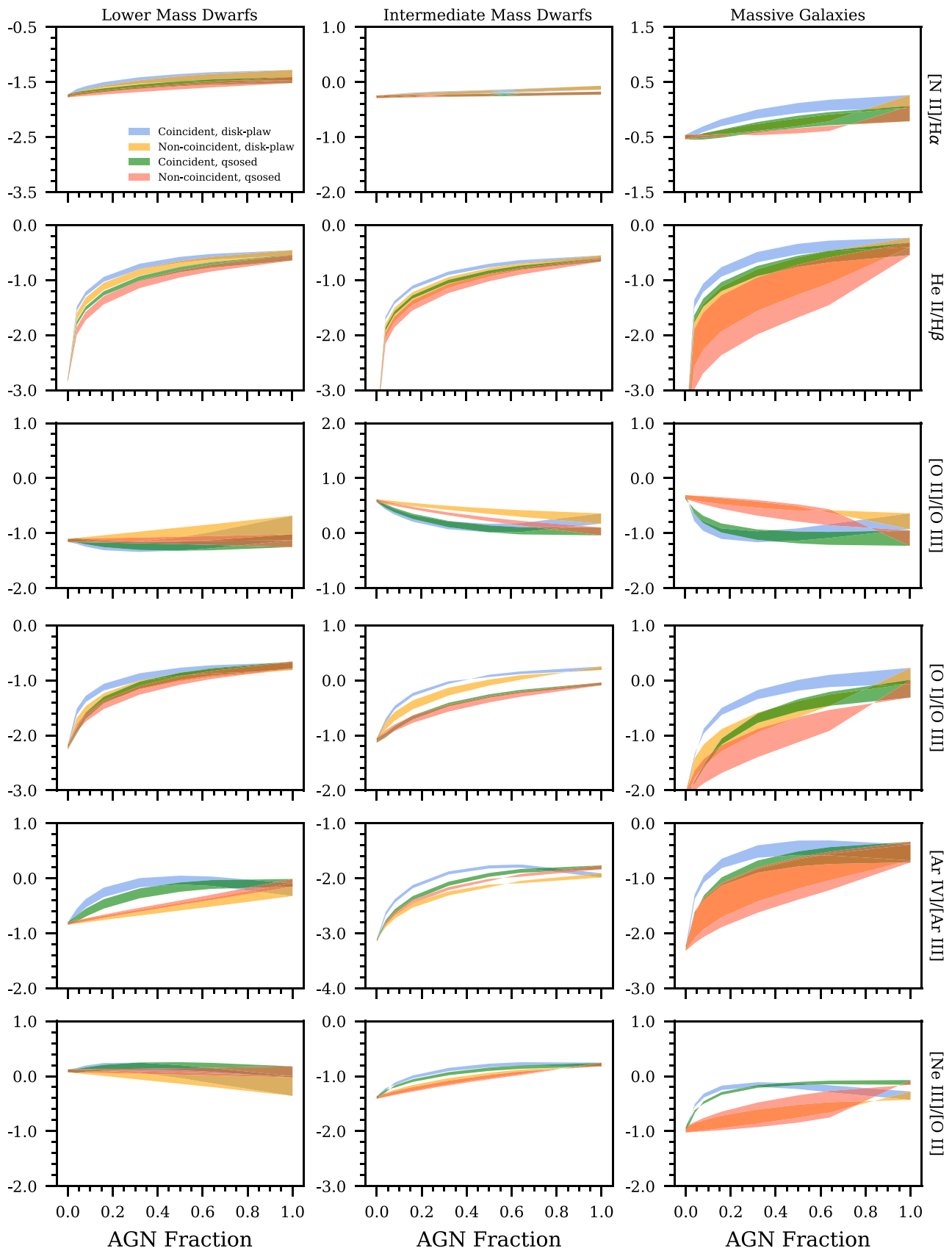


Figure 11. Additional optical emission line excitation diagnostics in the same format as Figure 5 with $M_{\text{BH}} = 10^5 M_{\odot}$.

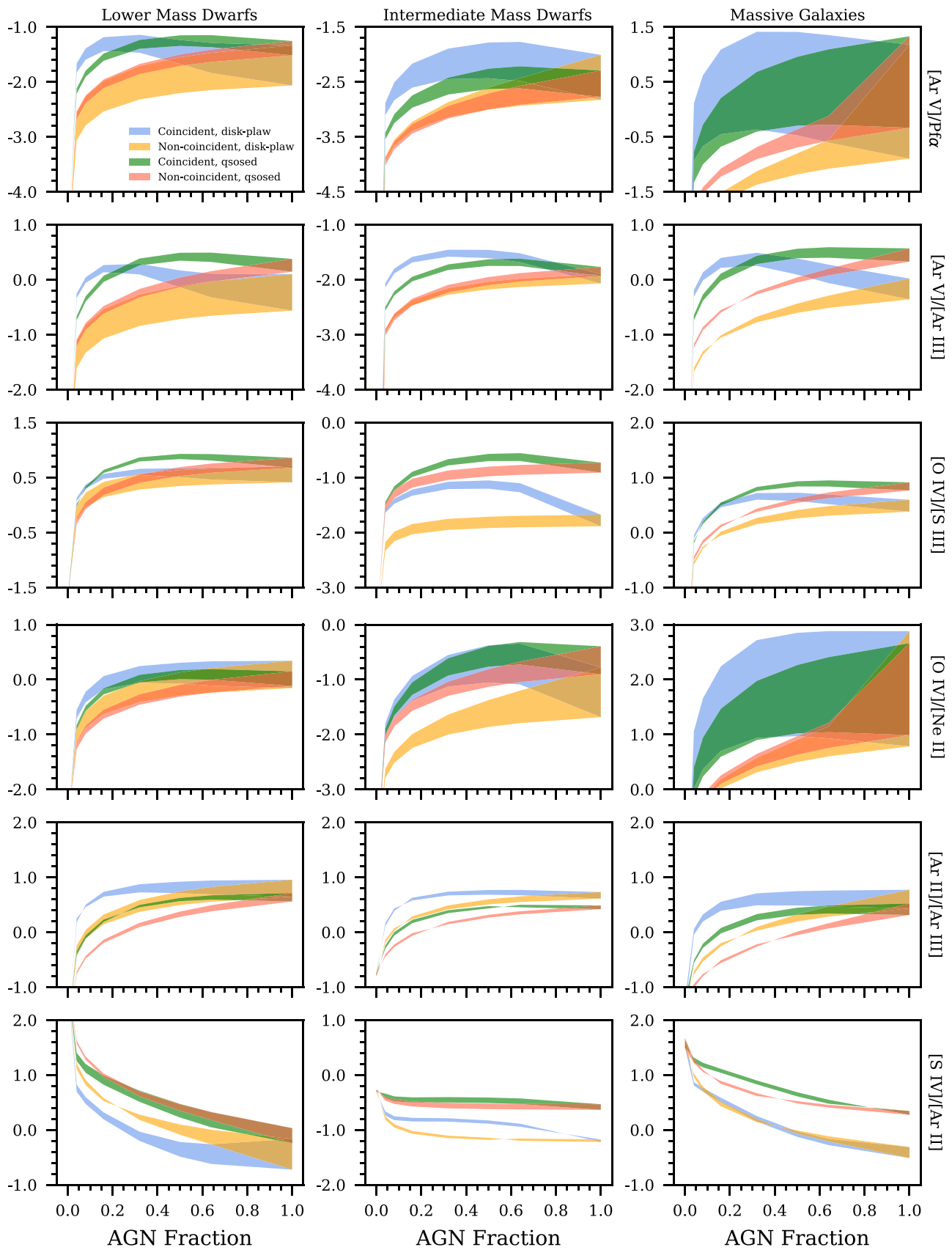


Figure 12. Additional mid-IR emission line excitation diagnostics in the same format as Figure 6 with $M_{\text{BH}} = 10^3 M_{\odot}$.

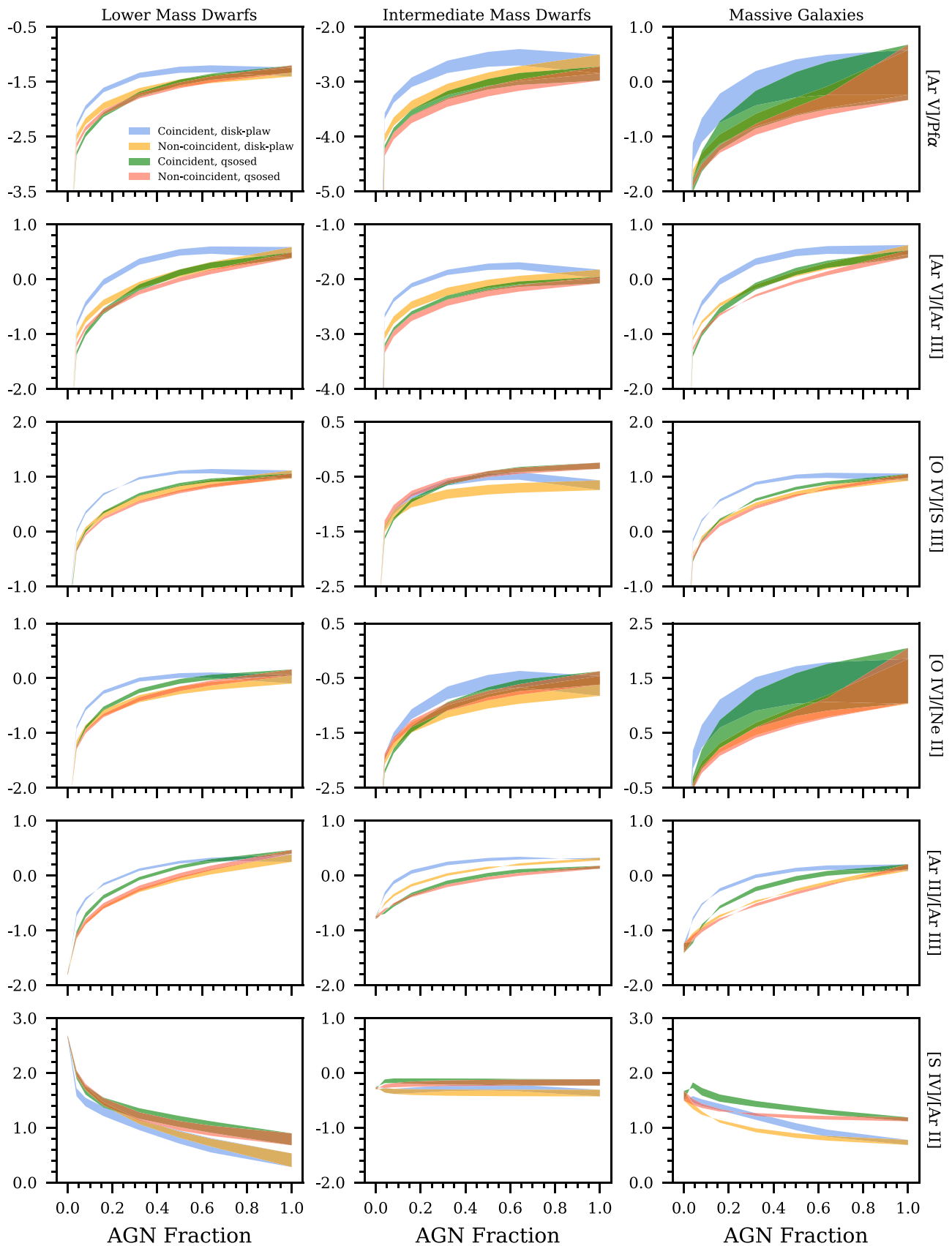


Figure 13. Additional mid-IR emission line excitation diagnostics in the same format as Figure 7 with $M_{\text{BH}} = 10^5 M_{\odot}$.

amounts of uncertainty for most regimes of galaxy masses. In contrast, [O IV]/[S III] and [Ar II]/[Ar III] provide suitable backups for [O IV]/Pf α and [Ar II]/Pf α (Figures 6 and 7) across the black hole masses and galaxy masses we have considered.

ORCID iDs

Chris T. Richardson  <https://orcid.org/0000-0002-3703-0719>
 Mugdha S. Polimera  <https://orcid.org/0000-0001-6162-3963>
 Sheila J. Kannappan  <https://orcid.org/0000-0002-3378-6551>
 Jillian M. Bellovary  <https://orcid.org/0000-0001-7596-8372>

References

- Abel, N. P., Dudley, C., Fischer, J., Satyapal, S., & van Hoof, P. A. M. 2009, *ApJ*, 701, 1147
- Abel, N. P., van Hoof, P. A. M., Shaw, G., Ferland, G. J., & Elwert, T. 2008, *ApJ*, 686, 1125
- Adhikari, T. P., Rózańska, A., Czerny, B., Hryniewicz, K., & Ferland, G. J. 2016, *ApJ*, 831, 68
- Amayo, A., Delgado-Inglada, G., & Stasińska, G. 2021, *MNRAS*, 505, 2361
- Arcodia, R., Ponti, G., Merloni, A., & Nandra, K. 2020, *A&A*, 638, A100
- Baldwin, J. A., Ferland, G. J., Martin, P. G., et al. 1991, *ApJ*, 374, 580
- Baldwin, J. A., Phillips, M. M., & Terlevich, R. 1981, *PASP*, 93, 5
- Barker, E. S., Lugger, P. M., Weiler, E. J., & York, D. G. 1984, *ApJ*, 280, 600
- Barth, A. J., Ho, L. C., Rutledge, R. E., & Sargent, W. L. W. 2004, *ApJ*, 607, 90
- Bautista, M. A. 1999, *ApJ*, 527, 474
- Bellovary, J. M., Hayoune, S., Chafra, K., et al. 2021, *MNRAS*, 505, 5129
- Bhat, H. K., Chakravorty, S., Sengupta, D., et al. 2020, *MNRAS*, 497, 2992
- Bohn, T., Canalizo, G., Veilleux, S., & Liu, W. 2021, *ApJ*, 911, 70
- Brinchmann, J., Kunth, D., & Durret, F. 2008, *A&A*, 485, 657
- Cann, J. M., Satyapal, S., Abel, N. P., et al. 2019, *ApJL*, 870, L2
- Cann, J. M., Satyapal, S., Abel, N. P., et al. 2018, *ApJ*, 861, 142
- Chaffee, F. H. J., & White, R. E. 1982, *ApJS*, 50, 169
- Cormier, D., Madden, S. C., Leboutteiller, V., et al. 2015, *A&A*, 578, A53
- Cormier, D., Abel, N. P., Hony, S., et al. 2019, *A&A*, 626, A23
- Crinklaw, G., Federman, S. R., & Joseph, C. L. 1994, *ApJ*, 424, 748
- D'Agostino, J. J., Kewley, L. J., Groves, B., et al. 2019, *ApJ*, 878, 2
- Dale, D. A., Smith, J. D. T., Armus, L., et al. 2006, *ApJ*, 646, 161
- De Cia, A., Ledoux, C., Mattsson, L., et al. 2016, *A&A*, 596, A97
- Dekel, A., & Birboim, Y. 2006, *MNRAS*, 368, 2
- Desroches, L.-B., Greene, J. E., & Ho, L. C. 2009, *ApJ*, 698, 1515
- Dwek, E. 1998, *ApJ*, 501, 643
- Elvis, M. 2000, *ApJ*, 545, 63
- Federman, S. R., Sheffer, Y., Lambert, D. L., & Gilliland, R. L. 1993, *ApJL*, 413, L51
- Feltre, A., Charlot, S., & Gutkin, J. 2016, *MNRAS*, 456, 3354
- Ferguson, J. W., Korista, K. T., Baldwin, J. A., & Ferland, G. J. 1997, *ApJ*, 487, 122
- Ferland, G. J. 2001, *PASP*, 113, 41
- Ferland, G. J., Chatzikos, M., Guzmán, F., et al. 2017, *RMxAA*, 53, 385
- Geha, M., Blanton, M. R., Yan, R., & Tinker, J. L. 2012, *ApJ*, 757, 85
- Georgakakis, A., Salvato, M., Liu, Z., et al. 2017, *MNRAS*, 469, 3232
- Godet, O., Plazolles, B., Kawaguchi, T., et al. 2012, *ApJ*, 752, 34
- Goicoechea, J. R., & Cuadrado, S. 2021, *A&A*, 647, L7
- Grasha, K., Roy, A., Sutherland, R. S., & Kewley, L. J. 2021, *ApJ*, 908, 241
- Greene, J. E., Strader, J., & Ho, L. C. 2020, *ARA&A*, 58, 257
- Grevesse, N., Scott, P., Asplund, M., & Sauval, A. J. 2015, *A&A*, 573, A27
- Grupe, D., Komossa, S., Leighly, K. M., & Page, K. L. 2010, *ApJS*, 187, 64
- Gry, C., & Jenkins, E. B. 2017, *A&A*, 598, A31
- Gutkin, J., Charlot, S., & Bruzual, G. 2016, *MNRAS*, 462, 1757
- Hao, L., Wu, Y., Charmandaris, V., et al. 2009, *ApJ*, 704, 1159
- Hily-Blant, P., Pineau des Forêts, G., Faure, A., & Lique, F. 2021, *A&A*, 658, A168
- Hood, C. E., Barth, A. J., Ho, L. C., & Greene, J. E. 2017, *ApJ*, 838, 26
- Inami, H., Armus, L., Charmandaris, V., et al. 2013, *ApJ*, 777, 156
- Indriolo, N., Geballe, T. R., Oka, T., & McCall, B. J. 2007, *ApJ*, 671, 1736
- Jenkins, E. B. 2009, *ApJ*, 700, 1299
- Jenkins, E. B., & Wallerstein, G. 2017, *ApJ*, 838, 85
- Kannappan, S. J. 2004, *ApJL*, 611, L89
- Kannappan, S. J., & Wei, L. H. 2008, in AIP Conf. Ser. 1035, The Evolution of Galaxies Through the Neutral Hydrogen Window, ed. R. Minchin & E. Momjian (Cambridge: Cambridge Univ. Press), 163
- Kashino, D., & Inoue, A. K. 2019, *MNRAS*, 486, 1053
- Kauffmann, G., Heckman, T. M., Tremonti, C., et al. 2003, *MNRAS*, 346, 1055
- Kewley, L. J., Dopita, M. A., Leitherer, C., et al. 2013, *ApJ*, 774, 100
- Kewley, L. J., Dopita, M. A., Sutherland, R. S., Heisler, C. A., & Trevena, J. 2001, *ApJ*, 556, 121
- Kewley, L. J., Groves, B., Kauffmann, G., & Heckman, T. 2006, *MNRAS*, 372, 961
- Kimball, S. J., Reines, A. E., Schutte, Z., Greene, J. E., & Geha, M. 2021, *ApJ*, 911, 134
- Kimbro, E., Reines, A. E., Molina, M., Deller, A. T., & Stern, D. 2021, *ApJ*, 912, 89
- Kubota, A., & Done, C. 2018, *MNRAS*, 480, 1247
- Laas, J. C., & Caselli, P. 2019, *A&A*, 624, A108
- Lamareille, F., Mouhcine, M., Contini, T., Lewis, I., & Maddox, S. 2004, *MNRAS*, 350, 396
- Leboutteiller, V., Péquignot, D., Cormier, D., et al. 2017, *A&A*, 602, A45
- Mac Low, M.-M., & Ferrara, A. 1999, *ApJ*, 513, 142
- Magorrian, J., Tremaine, S., Richstone, D., et al. 1998, *AJ*, 115, 2285
- Mazzalay, X., Rodríguez-Ardila, A., & Komossa, S. 2010, *MNRAS*, 405, 1315
- Meléndez, M., Heckman, T. M., Martínez-Paredes, M., Kraemer, S. B., & Mendoza, C. 2014, *MNRAS*, 443, 1358
- Meskhidze, H., & Richardson, C. T. 2017, *Ap&SS*, 362, 200
- Mitsuda, K., Inoue, H., Koyama, K., et al. 1984, *PASJ*, 36, 741
- Mullman, K. L., Lawler, J. E., Zsargó, J., & Federman, S. R. 1998, *ApJ*, 500, 1064
- Nicholls, D. C., Sutherland, R. S., Dopita, M. A., Kewley, L. J., & Groves, B. A. 2017, *MNRAS*, 466, 4403
- Nieva, M. F., & Przybilla, N. 2012, *A&A*, 539, A143
- Osterbrock, D. E., & Ferland, G. J. 2006, *Astrophysics of Gaseous Nebulae and Active Galactic Nuclei* (Sausalito, CA: Univ. Science Books)
- Panda, S., Czerny, B., Done, C., & Kubota, A. 2019, *ApJ*, 875, 133
- Peimbert, A., & Peimbert, M. 2010, *ApJ*, 724, 791
- Pellegrini, E. W., Baldwin, J. A., & Ferland, G. J. 2011, *ApJ*, 738, 34
- Peterson, B. M. 1997, *An Introduction to Active Galactic Nuclei* (Cambridge: Cambridge Univ. Press)
- Pinto, C., Kaastra, J. S., Costantini, E., & de Vries, C. 2013, *A&A*, 551, A25
- Reines, A. E., Condon, J. J., Darling, J., & Greene, J. E. 2020, *ApJ*, 888, 36
- Reines, A. E., & Volonteri, M. 2015, *ApJ*, 813, 82
- Rémy-Ruyer, A., Madden, S. C., Galliano, F., et al. 2014, *A&A*, 563, A31
- Richardson, C. T., Allen, J. T., Baldwin, J. A., Hewett, P. C., & Ferland, G. J. 2014, *MNRAS*, 437, 2376
- Richardson, C. T., Allen, J. T., Baldwin, J. A., et al. 2016, *MNRAS*, 458, 988
- Richardson, C. T., Polimera, M. S., Kannappan, S. J., Moffett, A. J., & Bittner, A. S. 2019, *MNRAS*, 486, 3541
- Riffel, R., Rodríguez-Ardila, A., & Pastoriza, M. G. 2006, *A&A*, 457, 61
- Roman-Duval, J., Jenkins, E. B., Williams, B., et al. 2019, *ApJ*, 871, 151
- Sarkar, A., Ferland, G. J., Chatzikos, M., et al. 2021, *ApJ*, 907, 12
- Satyapal, S., Abel, N. P., & Secrest, N. J. 2018, *ApJ*, 858, 38
- Satyapal, S., Kamal, L., Cann, J. M., Secrest, N. J., & Abel, N. P. 2021, *ApJ*, 906, 35
- Savage, B. D., & Sembach, K. R. 1996, *ARA&A*, 34, 279
- Sazonov, S., Churazov, E., & Krivonoz, R. 2015, *MNRAS*, 454, 1202
- Scott, P., Asplund, M., Grevesse, N., Bergemann, M., & Sauval, A. J. 2015a, *A&A*, 573, A26
- Scott, P., Grevesse, N., Asplund, M., et al. 2015b, *A&A*, 573, A25
- Senchyna, P., Stark, D. P., Mirocha, J., et al. 2020, *MNRAS*, 494, 941
- Simmonds, C., Schaerer, D., & Verhamme, A. 2021, *A&A*, 656, A127
- Snow, T. P. J., & Dodgen, S. L. 1980, *ApJ*, 237, 708
- Snow, T. P., Destree, J. D., & Jensen, A. G. 2007, *ApJ*, 655, 285
- Stanway, E. R., Eldridge, J. J., & Becker, G. D. 2016, *MNRAS*, 456, 485
- Stasińska, G., Izotov, Y., Morisset, C., & Guseva, N. 2015, *A&A*, 576, A83
- Sturm, E., Lutz, D., Verma, A., et al. 2002, *A&A*, 393, 821
- Sutherland, R. S., & Dopita, M. A. 2017, *ApJS*, 229, 34
- Tchernyshyov, K., Meixner, M., Seale, J., et al. 2015, *ApJ*, 811, 78
- Thomas, A. D., Dopita, M. A., Kewley, L. J., et al. 2018, *ApJ*, 856, 89
- Tremonti, C. A., Heckman, T. M., Kauffmann, G., et al. 2004, *ApJ*, 613, 898
- Veilleux, S., & Osterbrock, D. E. 1987, *ApJS*, 63, 295
- Weaver, K. A., Meléndez, M., Mushotzky, R. F., et al. 2010, *ApJ*, 716, 1151
- White, R. E. 1986, *ApJ*, 307, 777
- Xiao, L., Stanway, E. R., & Eldridge, J. J. 2018, *MNRAS*, 477, 904
- York, D. G., Meneguzzi, M., & Snow, T. P. 1982, *ApJ*, 255, 524